Surface topography and internal strain variation in wide hot orogens from three-dimensional analogue and two-dimensional numerical vice models

ALEXANDER R. CRUDEN, MOHAMMAD H. B. NASSERI & RUSSELL PYSKLYWEC
Department of Geology, University of Toronto, 22 Russell Street, Toronto, Ontario M5S 3B1, Canada

Abstract: The post-accretionary deformation of wide, hot orogens is characterized by pure-shear or transpressional shortening of relatively weak lithosphere (the orogen) between converging stronger blocks (the vice). We report on a series of analogue vice models and compare the resulting three-dimensional strain fields and surface topographies to equivalent two-dimensional numerical experiments. In the analogue models a rheologically stratified (frictional/viscous) weak orogenic lithosphere overlying a viscous asthenosphere is squeezed between converging strong lithospheric blocks. Ductile lower crust and mantle in the weak lithosphere is free to flow laterally, parallel to the orogen. The Argand number describes the model dynamics and strongly controls both the orogenic relief and the degree of lower crustal orogen parallel stretching in the analogue models. Cross sections of numerical and analogue experiments display consistent geometries in which upper crustal deformation is characterized by upright folding compared to apparently decoupled horizontal strains in the lower crust. The relative buoyancy and degree of orogen parallel flow in the lower crust of the analogue models has a dramatic influence on three-dimensional strain fields and the kinematics of upper crustal curvilinear shear zones. The analogue and numerical results demonstrate the importance of three-dimensional effects in determining the structure of natural orogens and compare favourably to field and geophysical observations of large hot orogens in the geological record.

Three-dimensional strain partitioning has long been recognized as a key phenomenon in the kinematic and dynamic evolution of convergent orogens (e.g., Oldow *et al.* 1989; Vauchez & Nicolas 1991; Royden 1996). A classic example is the partitioning between orogen-parallel strike-slip fault systems and ductile thickening in the Alpine-Himalayan chain (e.g., Tapponnier *et al.* 1982; Dewey *et al.* 1986; Davy & Cobbold 1988). Recent studies have documented decoupling between upper crustal and mid- to lower-crustal deformation in convergent magmatic arc, collisional orogen and post-orogenic collapse settings (e.g., Axen *et al.* 1998; Garde *et al.* 2002; Klepeis *et al.* 2004). A common expression of such decoupling is the observation of vertical orogen sub-parallel transpression zones, upright folding and cleavage development in the upper crust versus subhorizontal fabric development and lateral flow in the mid to lower crust, as documented by both field and seismic reflection studies in Archean to Mesozoic orogens (e.g., Collins & Vernon 1991; Gapais *et al.* 1992; Jackson & Cruden 1995; Hajnal *et al.* 1996; Moser *et al.* 1996; Royden *et al.* 1997; Axen *et al.* 1998).

The post-accretionary deformation of such wide, hot orogens (e.g., Superior, Grenville, Variscan, Cordilleran, Tibetan) has been attributed to pure-shear or transpressional shortening of relatively weak lithosphere (the orogen) between converging stronger blocks (the vice). In such 'vice models', the orogenic crust is weakened due to the properties of inherited accreted material or thermal/magmatic softening, and deformation is effectively decoupled from mantle dynamics (Ross *et al.* 1995; Ellis *et al.* 1998; Burg *et al.* 2002). The structural and topographic development of the resulting orogen depends on the vertical and lateral rheological structure of the lithosphere, the initial and final widths of the weak zone, surface erosion, and three-dimensional effects (e.g., lateral extrusion; Dewey *et al.* 1986; Ratschbacher *et al.* 1991; Mancktelow & Pavlis 1994; Royden 1996; Seyferth & Henk 2004).

The purpose of this contribution is to investigate the roles of orogen parallel flow and rheological stratification on the vertical and lateral

From: BUITER, S. J. H. & SCHREURS, G. (eds) 2006. *Analogue and Numerical Modelling of Crustal-Scale Processes*. Geological Society, London, Special Publications, **253**, 79–104.
0305-8719/06/$15.00

development of structures in convergent settings. We describe a series of three-dimensional (3D) analogue model experiments and corresponding two-dimensional (2D) numerical models that investigate the structural and topographic response of a model orogenic lithosphere as it is compressed between converging blocks of significantly stronger lithosphere. The analogue experiments inherently permit flow of orogenic material orthogonal to the compression direction. Comparison of these experiments with 2D numerical models, together with detailed structural and topographic data from the model surface and serial sectioning allows us to evaluate the significance of such orogen parallel flow. We will highlight the influence of relative variations in the strength and density of the ductile crust, which dictate the degree of coupling within the crust and body forces, respectively.

Experimental design

The basic design of both our analogue and numerical experiments follows the set up of the original vice models of Ellis *et al.* (1998) and is also similar to recent 3D numerical models of Seyferth and Henk (2004). Due to restrictions imposed by laboratory modelling techniques, our experiments are isothermal, which contrasts with those of Ellis *et al.* (1998) and Seyferth and Henk (2004). However, our focus is to explore the first-order effects of syn-convergent, orogen parallel flow rather than time-dependent phenomena due to variations in thermal and rheological structure. Hence the isothermal nature of our experiments is justified, and the results presented below are complementary to published 2D and 3D numerical thermomechanical models.

The basic configuration of our analogue and numerical experiments is summarized in Figure 1. In the 3D analogue models, a relatively weak model orogenic lithosphere composed of brittle material (upper crust) overlying viscous layers representing ductile lower crust and mantle lithosphere is squeezed between blocks (the vice) of model lithosphere of significantly greater total strength (Fig. 2). Both the vice and orogen float isostatically on a weaker model asthenosphere. Convergence is achieved by the motion of two pistons, which move inward at the same constant rate, driven by a step motor and screw gear assembly (Fig. 3). The vice-piston and vice-orogen boundaries are no-slip, as is the contact between asthenospheric material and the tank walls. The upper boundary in both the analogue and numerical models is a free surface.

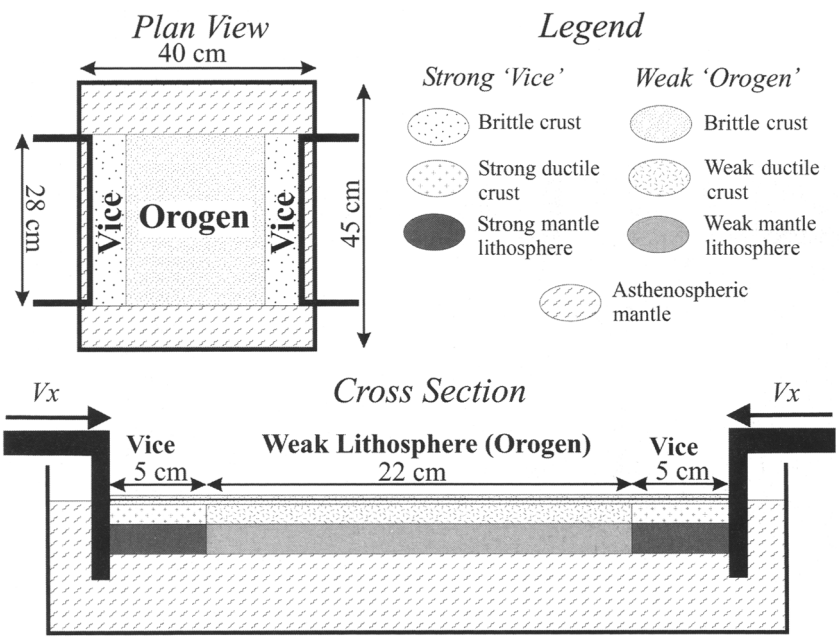

Fig. 1. Vice model set up. Top left is a plan view and bottom is a cross-sectional view of how each analogue experiment is constructed. With the exception of the rigid pistons (black) used to impose orogenic convergence in the analogue models, the cross-section also summarizes the set-up for the numerical experiments.

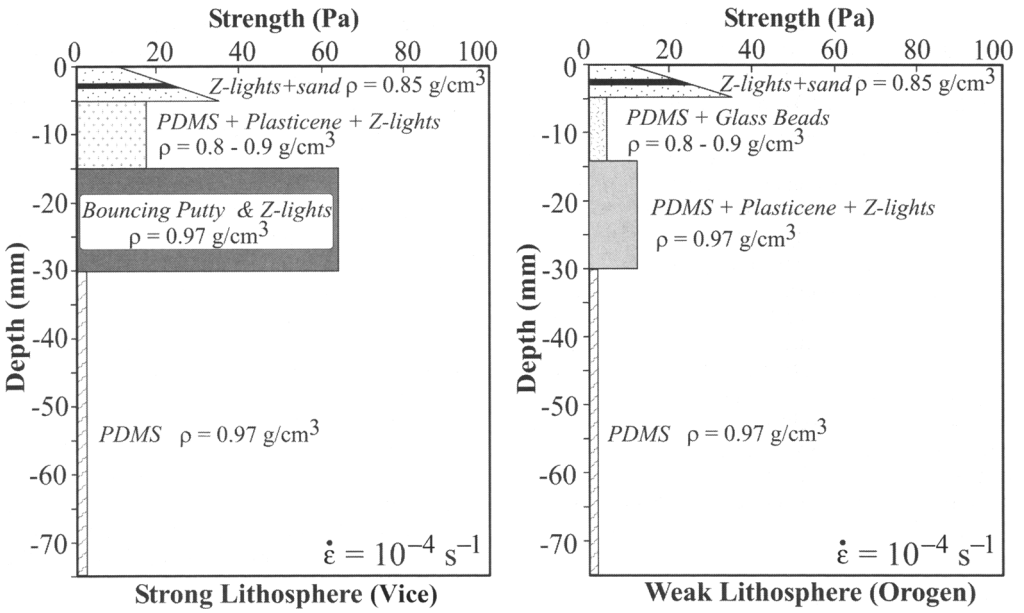

Fig. 2. Representative strength envelopes for the strong lithospheric blocks (vice) and weak orogenic lithosphere employed in the analogue experiments. See Table 1 for a complete summary of the physical properties of materials employed in the experiments.

Orogen parallel flow in the analogue experiments is achieved by constructing the model orogen such that it is unconfined at both ends (Figs 1 and 3). As such, the model orogen is free to flow outwards into a reservoir that is initially filled only with asthenospheric material. A similar approach has been used previously to model radially spreading nappes (Gilbert & Merle 1987; Merle 1989), and indentor (Davy & Cobbold 1988) and escape tectonics (Ratschbacher *et al.* 1991). In nature such unconfined boundaries might be represented by subduction zones, which retreat away from the orogen due to slab roll back (e.g., Schellart & Lister 2004). Lateral flow of model asthenosphere material in our simulated tectonic vice is illustrated in Figure 4. Deformation of a passive marker grid indicates that bulk orogen normal contractional and orogen parallel extensional strain is effectively homogeneous in the area of the models underlain by orogenic lithosphere. More complex strain fields develop adjacent to the lateral walls of the tank and at the corners of the pistons, outside the area of experimental interest. Because asthenospheric material is free to move around and under the pistons (Fig. 4), there is no change of volume or depth of this layer throughout the tank during the experiment.

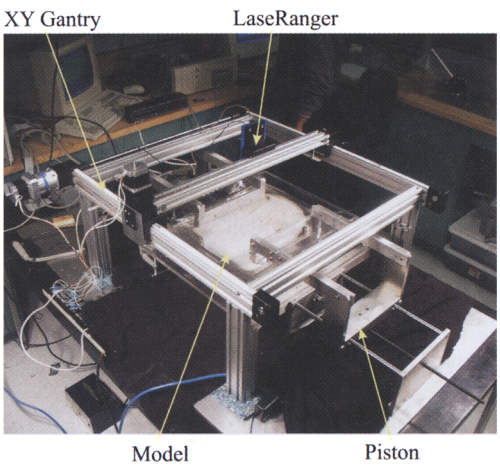

Fig. 3. Oblique view of the experimental apparatus and laser topography scanner. Both the piston and XY-gantry are propelled by computer-controlled stepper motors. Person and control computer in background for scale.

The 2D numerical models are set up with identical cross-sectional geometry and material properties to those of the analogue experiments. Our approach to modelling takes advantage of the relative strengths of laboratory and numerical approaches (e.g., Pysklywec & Cruden 2004).

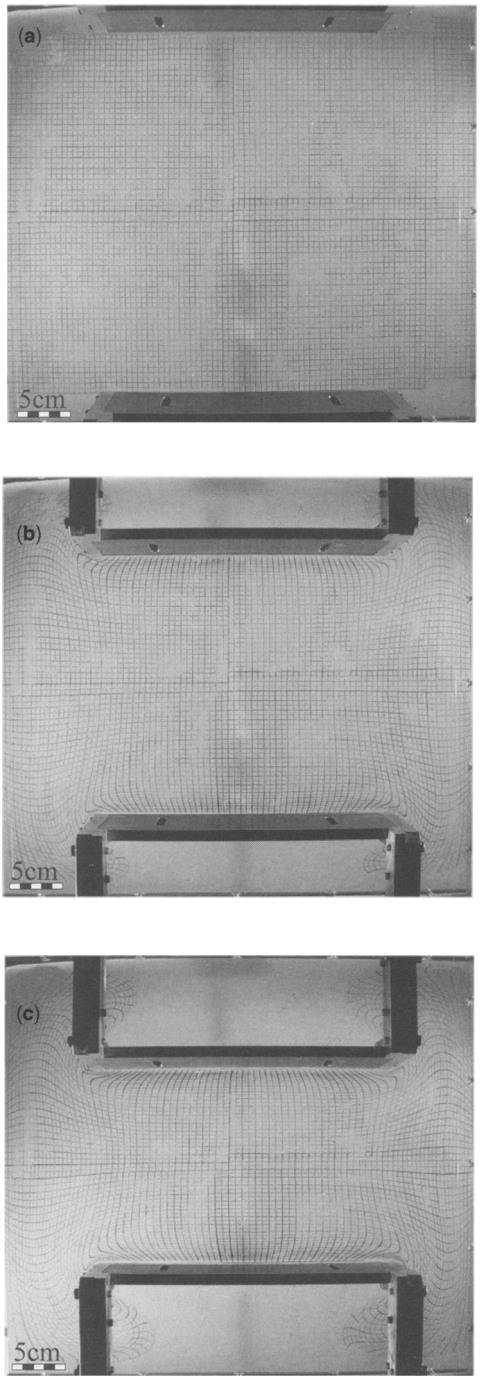

Fig. 4. Deformation of passive marker grid at top of asthenospheric material in response to convergence of pistons. The displacement of the passive grid gives an approximate illustration of the flow of model asthenosphere beneath fully constructed vice models.

In the vice experiments reported here, analogue models provide insights into the contribution of 3D orogen flow on the structural development of the orogen. The 2D numerical experiments act as a control on the laboratory experiments, by allowing for more variations in rheological parameters, and providing quantitative information on the evolving model orogen through time.

Laboratory experiments

Scaling and the general construction of the laboratory experiments (Table 1; Figs 1 and 2) follows the approach for analogue modelling of lithospheric deformation at 1 g described by Davy and Cobbold (1988, 1991). The experiments are approximately scaled to nature by selection of appropriate dimensions (geometric similarity) and laboratory materials (dynamic and kinematic similarity). By necessity the scaling is only approximate because of practical considerations in the laboratory (limitations of model size, time and suitable materials) and uncertainties in the natural system (densities, rheologies, time dependence, etc.).

Materials and scaling

In designing the laboratory experiments we used the physical properties of the asthenospheric mantle material and the length scale of the crust as our principal constraints. For practical purposes we define a length scale based on a model crustal thickness, $l_m =$ 1.5 cm, which for a natural continental crustal thickness $l_p = 40$ km gives a length scale ratio $L = l_m/l_p = 3.8 \times 10^{-7}$ (where the subscripts m and p refer to laboratory and natural prototype scales, respectively). As our working fluid to model asthenospheric mantle we use polydimethylsiloxane (PDMS), which is a transparent, high viscosity, high molecular weight silicone polymer that is frequently used in analogue modelling studies (e.g., Weijermars 1986; Pysklywec & Cruden 2004). PDMS has a density $\rho_m =$ 970 kg/m^3, which for a natural asthenospheric density of $\rho_p = 3100$ kg/m^3, sets a density scale of $P = \rho_m/\rho_p = 0.31$. In these experiments at 1 g the gravity scale ratio is $G = g_m/g_p = 1.0$.

The rheological properties of all ductile materials used in this study were measured over a range of strain rates relevant to the experiments with a rotary viscometer (based on a design by Cobbold & Jackson 1992), calibrated against a TA Instruments AR1000 rheometer. PDMS has a slightly non-Newtonian rheology

Table 1. *Parameters for laboratory vice models*

		W (cm)	L (cm)	h (cm)	ρ (kg/m^3)	η_{eff} (Pas)	ϕ	σ_o (Pa)	Material	V_x (cm/hr)	S (cm)	F_t (Pa)	F_b (Pa)	Ar
All Models														
Asthenosphere	Mantle	32	45	4.5	970	2.50×10^4			PS			*c.* 50	*c.* 20	*c.* 0.4
Vice	Lower Crust	5	28	1.0–0.8	900	3.20×10^5			PS + Pl + Gb					
	Mantle Lithosphere	5	28	1.5–2.0	970	$>1.00 \times 10^7$			BP + Zl					
Individual Models														
Experiment #27	Upper Crust	32	28	0.6	850		28°–34°	7–44	S + Zl	1.6	9.6	6.8	25.2	3.7
	Lower Crust	22	28	1	900	5.20×10^4			PS + Zl					
	Mantle Lithosphere	22	28	1.5	970	1.58×10^4			PS + Pl + Zl					
Experiment #29	Upper Crust	32	28	0.6	850		28°–34°	7–44	S + Zl	1.1	7.7	6.3	25.3	4
	Lower Crust	22	28	1	800	4.05×10^4			PS + DF + Gb					
	Mantle Lithosphere	22	28	1.5	970	1.68×10^5			PS + Pl + Zl					
Experiment #30	Upper Crust	32	28	0.4	850		28°–34°	7–44	S + Zl	1	7.5	4.1	16.8	4.1
	Lower Crust	22	28	1	900	4.10×10^4			PS + DF + Gb					
	Mantle Lithosphere	22	28	1.5	970	1.71×10^5			PS + Pl + Zl					
Experiment #32	Upper Crust	32	28	0.4	840		28°–34°	7–44	S + Zl	0.4	11	3.2	16.7	5.2
	Lower Crust	22	28	0.8	900	4.28×10^4			PS + DF + Gb					
	Mantle Lithosphere	22	28	2	970	2.00×10^5			PS + Pl + Zl					
Experiment #33	Upper Crust	32	28	0.4	840		28°–34°	7–44	S + Zl	0.4	11	3.2	16.8	5.2
	Lower Crust	22	28	0.8	800	4.11×10^4			PS + DF + Gb					
	Mantle Lithosphere	22	28	2	970	2.00×10^5			PS + Pl + Zl					
Experiment #34	Upper Crust	32	28	0.45	850		28°–34°	7–44	S + Zl	1.3	8.45	4.8	19	4
	Lower Crust	22	28	0.8	900	1.17×10^4			PS + DF + Gb					
	Mantle Lithosphere	22	28	2	970	1.64×10^5			PS + Pl + Zl					

W = orogen perpendicular width; L = orogen parallel length; h = vertical thickness; ρ = density; η_{eff} = effective viscosity; ϕ = angle of internal friction; σ_o = cohesion (maximum values); Vs = convergence rate; S = amount of shortening; F_t = tectonic force (resistance); F_b = Bouyancy force (gravity collapse); Ar = Argand number = F_b/F_t.
PS = Polydimethylsiloxane (PDMS); Pl = Harbuts plasticene (blue/black); DF = Dow Corning 30,000 cSt Fluid; BP = Dow Corning Bouncing Putty; Gb = 3M Glass Bubbles; S = quartz sand; Zl = 3M Z-light ceramic microspheres.

defined by the flow law:

$$\sigma^n = \eta\,\dot{\varepsilon} \qquad (1)$$

where σ is stress, $\dot{\varepsilon}$ is strain rate, η is a material constant and n is the power law exponent. Because our modelling materials are slightly non-Newtonian ($n = 1.05$ to 1.2) for scaling purposes we define an effective dynamic viscosity $\eta_{\text{eff}} = \sigma/\dot{\varepsilon}$, which for our PDMS (Dow Corning Silastic 4-2901) at a laboratory strain rate of $10^{-5}\,\text{s}^{-1}$ is 2.5×10^4 Pa s. Assuming an effective viscosity of $[\eta_{\text{eff}}]_p = 10^{21}$ Pa s for the natural asthenosphere (Mitrovica & Forte 1997) defines a viscosity scale ratio $M = [\eta_{\text{eff}}]_m/[\eta_{\text{eff}}]_p = 2.5 \times 10^{-17}$. The time scale ratio for the experiments can now be defined as $T = M/[PLG] = t_m/t_p = 2.13 \times 10^{-10}$.

Thicknesses and properties of the crustal and mantle components of the model lithospheres follow from these scaling parameters and are summarized in Table 1 and Figures 1 and 2. Equivalent values of all experimental parameters are given in Table 2.

Variations in the both the density and effective viscosity of ductile mantle lithosphere and lower crust in the experiments are achieved by adding appropriate amounts of Harbut's plasticene (blue and black), low viscosity PDMS (Dow Corning 30,000 cSt Fluid) and solid fillers to PDMS. The effect of blending plasticene with PDMS is to increase both the density and effective viscosity of the mixture. Solid fillers employed in this study are 3M Z-lights ceramic microspheres and 3M Scotchlight Glass Bubbles, which have grain densities of 650 and 320 kg/m^3, respectively. Mixing different proportions of these fillers, which have average diameters *c.* 100 μm, to either pure PDMS or PDMS + Plasticene mixtures decreases the density and increases the effective viscosity of the material. Low viscosity PDMS can be added in small amounts to the above mixtures in order to lower their viscosity. Several different configurations of crustal density and effective viscosity structure were employed in our experiments (Table 1).

Brittle behaviour of the upper crust in the models is simulated by a layer of granular material, whose scaled thickness varies between models from 16 to 11 km. To acquire the desired average upper crustal density we alternated, in the appropriate proportion, layers of Z-light microspheres and quartz sand with bulk densities of 440 and 1570 kg/m^3, respectively. Ring shear tests on both materials in the normal stress range 500 to 2000 Pa determined internal friction angles $\phi = 28°$–$34°$ and (linearly extrapolated) cohesion values of $\sigma_o = 7$–44 Pa for Z-lights and quartz sand, respectively (J. Lohrmann, GeoForshungsZentrum, Potsdam, unpublished results 2005). Following Schellart (2000) we consider the cohesion values above to be upper bounds on the conditions in our experiments, in which normal stress values vary between 0 and 50 Pa. In this range, the cohesion of dry granular materials approaches 0 Pa (Schellart 2000), hence Z-lights and quartz sand are approximate analogues for modelling the macroscopic, frictional, behaviour of fractured upper crust (Davy & Cobbold 1991; Rossi & Storti 2003).

Model construction

All laboratory experiments were run in a 40 cm (width) × 45 cm (length) × 10 cm (depth) Plexiglas tank (Figs 1 and 3). Models were constructed by sequential addition of asthenospheric and lithospheric layers, with sufficient relaxation time allowed to minimize the development of air bubbles, and to ensure the pre-deformed model achieved isostatic equilibrium. During model construction, lateral flow of ductile material was prohibited by the insertion of vertical sheet metal barriers at the margins of the model orogen. These were removed immediately before the pistons were activated. After removal of the barriers and activation of the pistons, model orogenic material was free to flow at right angles to the compression direction into the reservoir of PDMS. This experimental set-up is designed to maximize the effects of orogen parallel flow driven primarily by piston convergence. Apart from a minor adjustment that occurs when the side barriers are removed, in the absence of piston convergence orogen parallel flow driven by gravity alone would be minimal over the typical duration of our experiments (*ca.* 8 hours).

Observation methods

Progress in all experiments was monitored by time-lapse digital photography from the side and top as well as by linear scanning of the surface topography (Fig. 3). A passive marker grid was imprinted on the top of the model by placing a rectilinear mask over the top surface and sprinkling a thin layer of fine grained white sand through it. Motion of this grid mapped progressive surface deformation in the evolution of the model. In the case of experiments employed to visualize the flow field in the asthenosphere, a passive marker grid was imprinted on the

Table 2. *Scaled natural equivalent parameters in vice models*

		W (km)	L (km)	h (km)	ρ (kg/m^3)	η_{eff} (Pas)	ϕ	σ_o (MPa)	V_x (cm/yr)	S (km)	F_t (MPa)	F_b (MPa)	Ar
All Models													
Asthenosphere	Mantle	853	747	120	3100	1.00×10^{21}					*c.* 420	*c.* 168	*c.* 0.4
Vice	Lower Crust	133	747	21–27	2876	1.28×10^{22}							
	Mantle Lithosphere	133	747	40–53	3100	4.00×10^{23}							
Individual Models													
Experiment #27	Upper Crust	853	747	16	2717		28°–34°	59–286	8.0	256	57	212	3.7
	Lower Crust	587	747	27	2876	2.08×10^{21}							
	Mantle Lithosphere	587	747	40	3100	6.32×10^{21}							
Experiment #29	Upper Crust	853	747	16	2717		28°–34°	59–286	5.5	205	53	213	4
	Lower Crust	587	747	27	2557	1.62×10^{21}							
	Mantle Lithosphere	587	747	40	3100	6.72×10^{21}							
Experiment #30	Upper Crust	853	747	11	2717		28°–34°	59–286	5.0	200	34	141	4.1
	Lower Crust	587	747	27	2876	1.64×10^{21}							
	Mantle Lithosphere	587	747	40	3100	6.84×10^{21}							
Experiment #32	Upper Crust	853	747	11	2685		28°–34°	59–286	2.0	293	27	140	5.2
	Lower Crust	587	747	21	2876	1.71×10^{21}							
	Mantle Lithosphere	587	747	53	3100	8.00×10^{21}							
Experiment #33	Upper Crust	853	747	11	2685		28°–34°	59–286	2.0	293	27	141	5.2
	Lower Crust	587	747	21	2557	1.64×10^{21}							
	Mantle Lithosphere	587	747	53	3100	8.00×10^{21}							
Experiment #34	Upper Crust	853	747	12	2717		28°–34°	59–286	6.5	225	40	160	4
	Lower Crust	587	747	21	2876	4.68×10^{20}							
	Mantle Lithosphere	587	747	53	3100	6.56×10^{21}							

Scaling factors = model/prototype: Length, $L = 3.8 \times 10^{7}$; Velocity, $V = 1760$; Density, $P = 0.313$; Viscosity, $M = 2.5 \times 10^{-17}$; Stress, $\Sigma = 1.19 \times 10^{-7}$; Time, $T = 2.13 \times 10^{-10}$.

PDMS using a transfer method (Dixon & Summers 1983).

Surface topography measurement was made using a laser triangulation device (Aculux LaseRanger) that is translated linearly over the model surface by an XY-gantry system at a stand-off distance of *c.* 13 cm (Fig. 3). Between 5 (Expt. #27) and 34 (Expt. #34) scan lines were collected at 0.5 to 1 hour intervals during the experiments (the variation was due to improvements made to the speed of data acquisition over the duration of the experimental programme). Individual topographic measurements were made with a spacing of 1 mm along each scan line and the positional accuracy of the XY gantry was $\pm 0.1 \sim$ mm. The distance resolution of the laser device is ± 0.1 mm, but due to gantry vibration and scattering effects of the model surface materials the nominal topographic resolution is $\pm 0.2 \sim$ mm.

The internal structure of models was examined after the end of each experiment. First, the granular layer over one third of the model surface was removed using a vacuum hose, and the exposed brittle ductile interface was photographed. Subsequently, the remaining granular material was saturated with water and the model was placed in a freezer at -50°C (i.e., below the crystallization temperature of PDMS). After 12 hours, serial sections of the model were prepared using a band saw, and photographed. Some viscous relaxation of deformed layer interfaces probably occurs during the initial cooling of the models. However, as shown below, the wavelengths and amplitudes of folded interfaces in the sectioned analogue models are similar to those observed in numerical experiments, indicating that the effects of viscous relaxation are relatively minor.

Numerical experiments

A suite of two-dimensional numerical experiments was conducted as a parallel comparison to the analogue models. The numerical models are scaled to the analogue experiments, and their initial configuration is shown in Figure 1.

The models assume incompressibility of the materials, and the governing equations for the system are:

$$-\nabla p + \nabla \cdot \sigma' + \rho g_z = 0 \qquad (2)$$

$$\nabla \cdot \mathbf{u} = 0 \qquad (3)$$

where $\mathbf{u}$ is the velocity field and g_z is the vertical component of gravity. The full stress tensor σ_{ij} has been divided into two components: $\sigma_{ij} = \sigma'_{ij} - p\delta_{ij}$ where σ' is the deviatoric component of the stress tensor and p is pressure ($p = -\frac{1}{3}\sigma_{ii}$ for an incompressible fluid). Viscous or plastic rheologies are imposed for the materials in the numerical model to simulate the behaviour of the analogue materials. For the viscous materials we adopt a power law constitutive relation (Eqn. 1), and for the brittle crust, a Coulomb-type yield criterion of the form $\sigma_y = p\sin\phi + \sigma_o$ was used (where σ_y is the second invariant of the deviatoric stress).

The system of equations is solved using the arbitrary Lagrangian–Eulerian (ALE) finite element method (Hirt *et al.* 1974; Fullsack 1995). The solution space is discretized using a Eulerian resolution of 321×81 nodes and a Lagrangian resolution of 601×151 nodes, evenly distributed through the box. The numerical routine has been benchmarked rigorously with previous studies (Poliakov & Podladchikov 1992; Blankenbach *et al.* 1989; Houseman & Molnar 1997; van Keken *et al.* 1997) to verify its accuracy in computing viscous flow and surface topography.

The top boundary of the box is a free surface and all the other sides have an imposed zero tangential velocity (i.e., no slip). Material is not permitted to penetrate the lower boundary of the box. Deformation in the model is driven by buoyancy forces arising from material density variations and the imposed lithospheric 'vice' contraction. This contraction is simulated as a velocity boundary condition at the sides of the solution space; along the lithospheric portion of each side boundary new lithosphere material is introduced into the box at a horizontal velocity $V_x/2$. An outward flux of asthenospheric material is imposed along the sub-lithospheric portion of the sidewalls of the box in order to balance the mass of injected lithosphere.

Overview and dynamic analysis of experiments

The six laboratory experiments reported here represent a range of orogenic conditions as dictated by rheological and density structure and boundary conditions (convergence rate, V_x). Variations in dynamics and body forces in the experiments can be quantified and direct comparison to nature can be made by considering the Argand number. The Argand number is defined as the dimensionless ratio of buoyancy forces to tectonic forces, $Ar = F_b/F_t$ (England & McKenzie 1982; Houseman & England 1986). For these experiments, the buoyancy

force is the static outward force per unit length that results in gravitational collapse of the model lithosphere over the asthenosphere. Following Benes & Davy (1996), the buoyancy force for a three-layer model is given by:

$$F_g = \rho_1 g \frac{h_1}{2} + \rho_1 g \frac{(z_2^2 - z_1^2)}{2} + \rho_1 g \frac{(z_3^2 - z_2^2)}{2} - g \frac{(\rho_1 h_1 + \rho_2 h_2 + \rho_3 h_3)}{2\rho_m} \quad (4)$$

where ρ_1, ρ_2, ρ_3 and h_1, h_2, h_3 are densities and thicknesses of the upper crust, lower crust and lithospheric mantle, respectively; ρ_m is the density of the asthenosphere (PDMS); $z_1 = h_1$, $z_2 = h_1 + h_2$, and $z_3 = h_1 + h_2 + h_3$. Note that F_g is calculated for the start of the experiment and therefore does not consider the buoyancy force caused by crustal thickness changes. F_g is therefore a relative measure of the potential for the model lithosphere to flow laterally over the asthenosphere, and it is resisted by F_t, which is the vertically averaged stress required to deform the model lithosphere at a given strain rate.

The tectonic force in the models is calculated as:

$$F_t = \frac{h_1\sigma_o + (h_1^2/2\tan\phi) + h_2(\eta_2\,\dot{\varepsilon})^{1/n_2} + h_3(\eta_3\,\dot{\varepsilon})^{1/n_3}}{z_3} \quad (5)$$

where η is the material constant, n is the power law exponent (Eqn 1; subscripts 1, 2, 3 refer to model upper crust, lower crust and lithospheric mantle, respectively) and $\dot{\varepsilon} = V_x/W$ where W is the width of the orogen measured parallel to the shortening direction. Note that because V_x is constant, $\dot{\varepsilon}$ increases with time during each experiment. As with F_g, values of F_t and Ar reported here are for the start of each experiment (Table 1).

F_t in the experimental orogen varies between 3.2 and 6.8 Pa, corresponding to natural values of 41 to 87 MPa (Tables 1 and 2). The main controls on F_t in the model orogen are due to the thickness of the brittle crust, h_1, and the effective viscosity of the lower crust, $[\eta_{\text{eff}}]_2$. With the exception of Experiment #34, the model orogenic mantle lithosphere is only marginally stronger than the lower crust. This was mainly predicated by limitations imposed by available analogue materials at the time the experiments were carried out, and the resulting trade-off between maintaining the correct density for the mantle lithosphere layer (important for body force scaling), and its strength. Although the effective viscosity of mantle lithosphere material in the experiments would certainly be too low for modelling of stable continental lithosphere, its relative strength compared to crustal and asthenospheric material is consistent with materials used in other analogue model studies (e.g., Sokoutis *et al.* 2000). The scaled natural effective viscosity of the mantle lithosphere in the experiments (*c.* 7×10^{21} Pa s; Table 2) is also consistent with experimental (e.g., Kohlstedt *et al.* 1995; Hirth & Kohlstedt 1996; Mackwell *et al.* 1998) and geophysics (e.g., Maggi *et al.* 2000) based estimates of the strength of upper mantle rocks in natural orogens, if the geothermal gradient is steep and conditions are relatively wet (e.g., $\eta_{\text{eff}} \sim 10^{21}$ to 10^{22} at strain rates of 10^{-14} to $10^{-15}\,\text{s}^{-1}$; Jackson 2002; Toussaint *et al.* 2004).

The strong lithospheric blocks (vice blocks) in the experiments have F_t values that are $\sim$10 times greater than the model orogen. The bulk of the strength in these blocks resides in the mantle lithosphere layer (Fig. 2), which is composed of bouncing putty with finite yield strength (Dixon & Summers 1986) mixed with Z-light spheres to achieve the correct density. The effective viscosities of the mantle lithosphere and lower crust in the vices scale up to $>1 \times 10^{23}$ and *c.* 1×10^{22} Pa s, respectively. These values are consistent with a dry upper mantle and granulitic lower crust (Kohlstedt *et al.* 1995; Mackwell *et al.* 1998), as could be expected in stable continental lithosphere. Hence the overall strength of the model orogenic and vice lithospheres and the details of their rheological structure are consistent with a hot orogen with a wet mantle lithosphere and quartz-dominated lower crust (e.g., Toussaint *et al.* 2004) being squeezed between blocks of cold cratonic continental lithosphere (Fig. 2; Table 2).

F_b in the experiments varies between 16.7 and 25.2 Pa, resulting in values of Ar from 3.7 and 5.2 (Fig. 5a; Table 1). Such values indicate that the orogenic lithosphere will tend to collapse if boundary conditions are suitable, and are consistent with conditions employed in previous numerical and analogue model studies of lithospheric convergence and extension (Houseman & England 1986; Benes & Davy 1996). Values of Ar between 1 and 10 are considered to describe the balance of forces in wide, hot orogens such as the Himalaya, and $Ar \geq 3$ is required to develop orogenic plateaux such as the Tibetan plateau (England & McKenzie 1982; Dewey *et al.* 1986; England & Houseman 1986). In the vice blocks, $Ar \ll 1$, which describes the balance of forces expected in stable continental lithosphere, in which gravitational forces are expected to be significantly resisted by the tectonic strength.

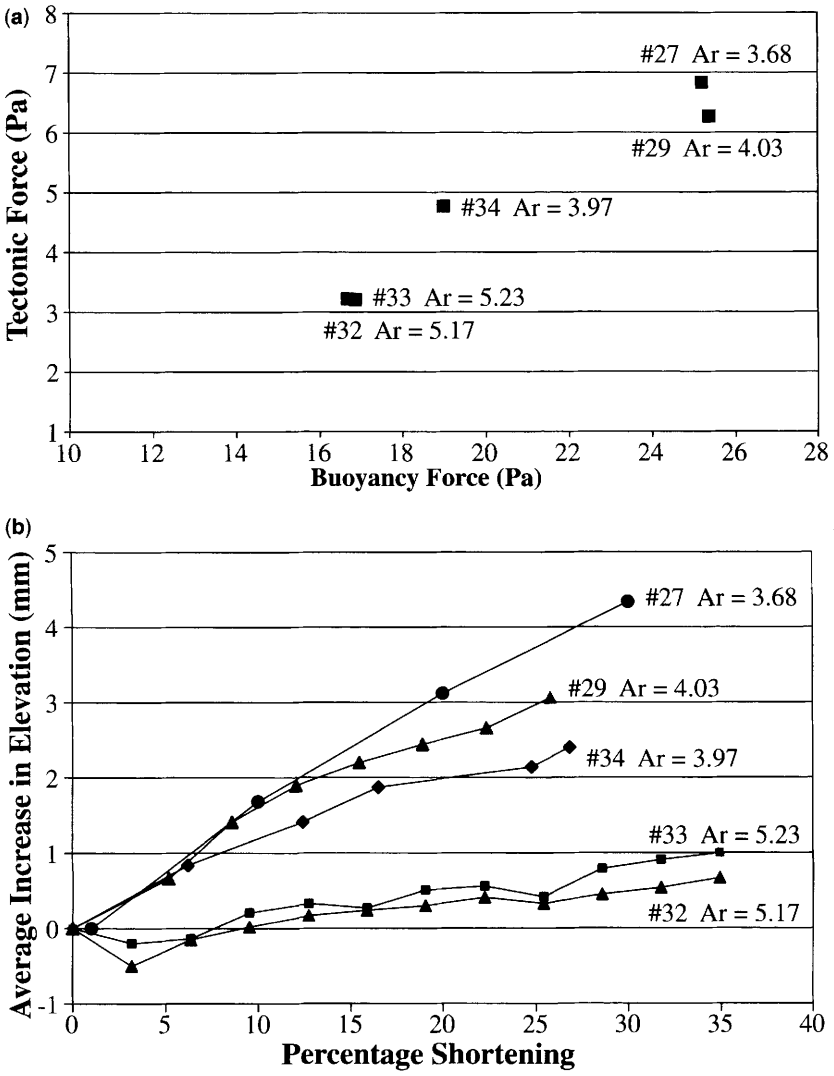

Fig. 5. (**a**) Comparison of tectonic forces (F_t) and buoyancy forces (F_b) in analogue experiments. (**b**) Increase of average surface elevation of orogenic crust in analogue vice models as a function of the amount (%) shortening and Argand number, *Ar*.

Because *Ar* in the experiments is in agreement with values estimated in nature, we can demonstrate approximate dynamic similarity between our vice models and wide, hot orogens. Kinematic similarity is satisfied by imposing model convergence rates of 0.4 to 1.6 cm/hr, which scale up to typical orogenic convergence rates of 2 to 8 cm/a. The model thicknesses and horizontal dimensions scale up to values expected in large orogenic systems (Table 2), which together with total scaled amounts of shortening of 200 to 300 km (25–35% shortening) also satisfy the requirements of geometric similarity.

The effect of *Ar* in the experiments can be evaluated by quantifying how elevation in the model orogen grows with time. Figure 5b plots the average elevation in the area confined between the vice blocks, determined by laser profilometry, as a function of the amount of shortening in each experiment. After an initial drop in elevation due to removal of the barriers at the edge of the model orogen, average elevation increases steadily. As expected, the

fastest elevation growth occurs in experiments with smaller *Ar* values. This is because orogenic thickening outstrips the rate of lateral orogenic collapse allowed by the strength of the model lithosphere. The average height attained in Experiment #27 corresponds to a scaled equivalent mean elevation of *c.* 11500 m, which seems excessive for terrestrial orogens. Experiments #29 and #34 have final scaled average elevations of *c.* 8000 and 6000 m, which is a reasonable fit for Earth, given the absence of erosion in the experiments. In the highest *Ar* experiments (#33 and #32), final scaled mean elevations are $\leq$2600 m and mean scaled elevations at times that correspond to the end of Experiments #29 and #34, are *c.* 1300 m.

In the presentation of the experimental results below, we will focus on the influence of *Ar* on the structural and topographic evolution of the model orogen, and examine the role of the relative buoyancy and strength of the lower crust. The attributes of the ductile crust of wide, hot orogens are important because the crust is likely to be weak due to the combined effects of high geothermal gradient, presence of water and quartz-rich composition (e.g., Toussaint *et al.* 2004). These conditions may also lead to partial melting over large areas (e.g., Meissner & Mooney 1998; Rey *et al.* 2001), resulting in a further lowering of the strength of the lower to mid-crust and, if the degree of melting is sufficient, to decrease its bulk density (e.g., Rey 1993; Teyssier & Whitney 2002). Experiments #29, #33 and #34 examine the situation of a weak, non-buoyant ductile crust; in Experiments #29 and #33, the ductile crust is weak and buoyant; and in Experiment #34 the ductile crust is non-buoyant, but significantly weaker than the other models.

Results

Firstly, we consider the influence of lower crustal density on the evolution of the models, using representative experiments having a buoyant (#29) or non-buoyant (#34) lower crust. Secondly, the contribution of *Ar* on experimental outcomes and the differences between equivalent 3D analogue and 2D numerical experiments are discussed by focussing on results of Experiments #29, #32 and #34.

Buoyant lower crust experiments (#29 and #33)

Surface deformation (analogue only), topography (analogue and numerical) and cross-sectional geometry (numerical only) of Experiment #29 at intermediate (12%) and late amounts (24%) of shortening are shown in Figure 6. Surface deformation in this experiment is characterized by early formation of a conjugate system of shear zones (Fig. 6a) that subsequently evolves into a localized, curvilinear orogen-subparallel zone of thrusting and folding (Figs 6a and 7a). Not evident in Figures 6a and d is the development of upper crustal folds, which are observed in the topographic profiles (Figs 6b and e) and serial sections (Fig. 8a). Overall, the amplitudes and wavelengths of the topographic features associated with these folds are very similar in the analogue and numerical runs. A notable feature in both the analogue and numerical runs of this experiment is the development of significant zones of overthrusting of the model orogen crust over the encroaching vice. A similar degree of overthrusting is also observed in Experiment #33, which also had a buoyant lower crust. Although upper crustal folding in Experiment #33 is more distributed than in Experiment #29, the formation of conjugate sets of upper crustal shear zones is also observed, particularly close to extruding margins of the model orogen.

In comparison to the experiments described below, overthrusting or 'overflow' parallel to the shortening direction at the vice margins, and the development of conjugate upper crustal shear zones within the orogen appear to be common attributes in models with buoyant ductile crust. We attribute the pronounced overflow of buoyant crust and overlying brittle material to be due to a 'water bed' effect. As postulated by Bailey (1999, 2001), a thickened, buoyant and weak ductile crust is gravitationally unstable. Under horizontal plane strain conditions, the resulting net outward force acts opposite to the shortening direction, and provided crustal strength can be exceeded at the orogen margins, overflow will occur (Bailey 2001). The effect of this overflow in our experiments is twofold. Firstly, as seen in the analogue and numerical cross sections (Fig. 8a), outwardly vergent thrust zones develop at the orogen-vice boundary zone. Secondly, upper crustal folding is suppressed because of orogen perpendicular extension caused by the overflow. In the analogue version of Experiment #29, folding in the orogen is confined to a central region, in which the folds are probably amplified by local gravitational instability between the upper and lower crust (Fig. 8a). In the equivalent numerical model, distributed upper crustal folds have significantly lower amplitude than in models with non-buoyant ductile crust. Formation of conjugate upper crustal shear zones in analogue Experiments #29 and #33 is consistent with

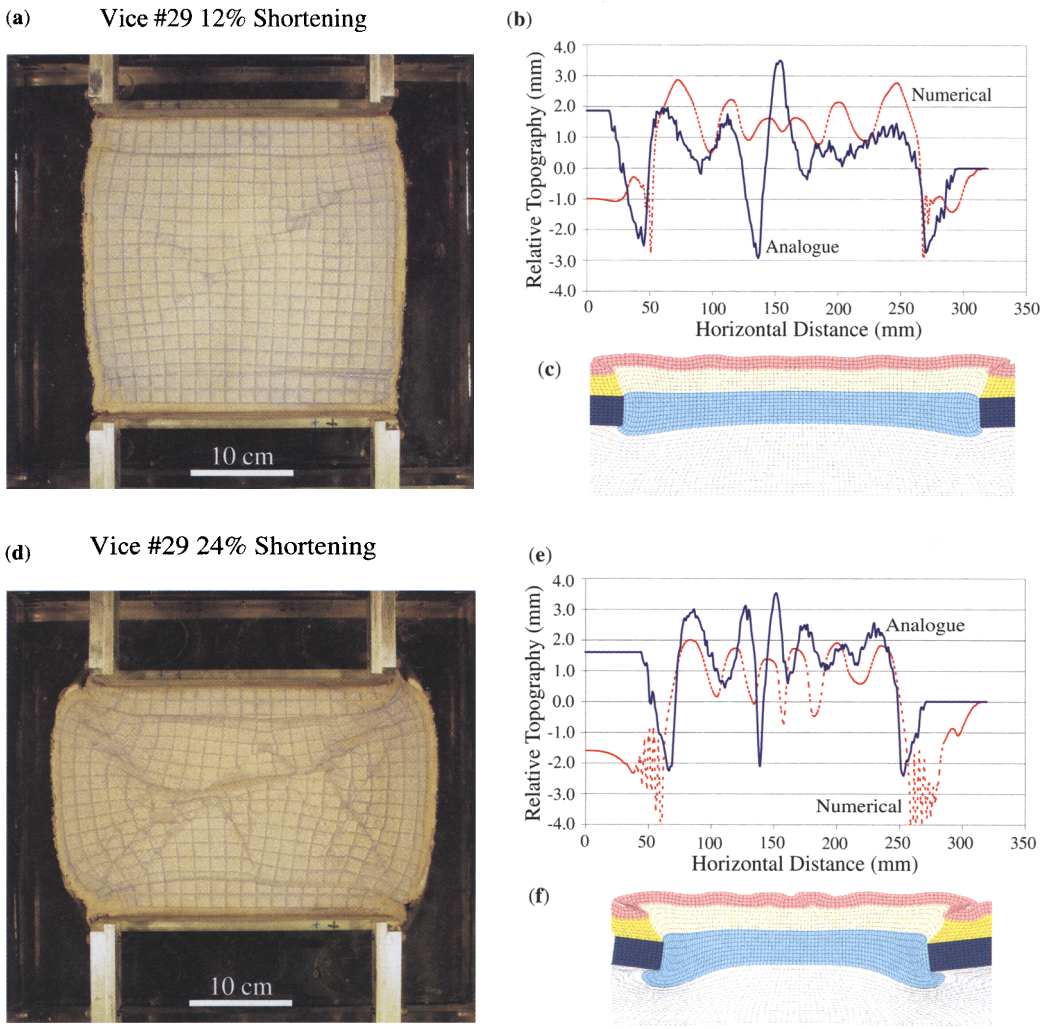

Fig. 6. Results for Experiment #29, with buoyant ductile crust. (**a**) and (**d**) Photographs of top surface after 12% and 24% shortening. (**b**) and (**e**) Comparison of central topographic profiles of analogue and numerical models after 12% and 24% shortening. Relative topography is the difference between the present and original elevation. The analogue and numerical results have been re-levelled for comparison purposes. (**c**) and (**f**) Cross-sections of numerical experiment at 12% and 24% shortening.

orogen parallel flow, driven both by the gravitationally unstable thickened ductile crust, and by orogen-parallel stretching exerted at the base of the model lithosphere by the asthenosphere (Fig. 4).

Due to the very high strength of the mantle lithosphere in the vice blocks, significantly weaker mantle lithosphere material in the model orogen has a tendency to underthrust the vice margins (Figs 6c, f and 8). This effect is observed in all experiments. We consider these features to be artefacts of the experimental boundary conditions and therefore do not ascribe any special tectonic significance to them. Their development does not appear to have a major influence on the formation of structures in the orogenic crust. However, the addition of extra dense material to the base of the vice lithosphere, together with a torque exerted on the strong vice upper mantle layer by the underthrusting of orogenic material, results in a net tilting of the vice blocks towards the interior of the model, as observed in both surface elevation data (Figs 6 and 9) and cross-sections (Fig. 8). Tilting of the

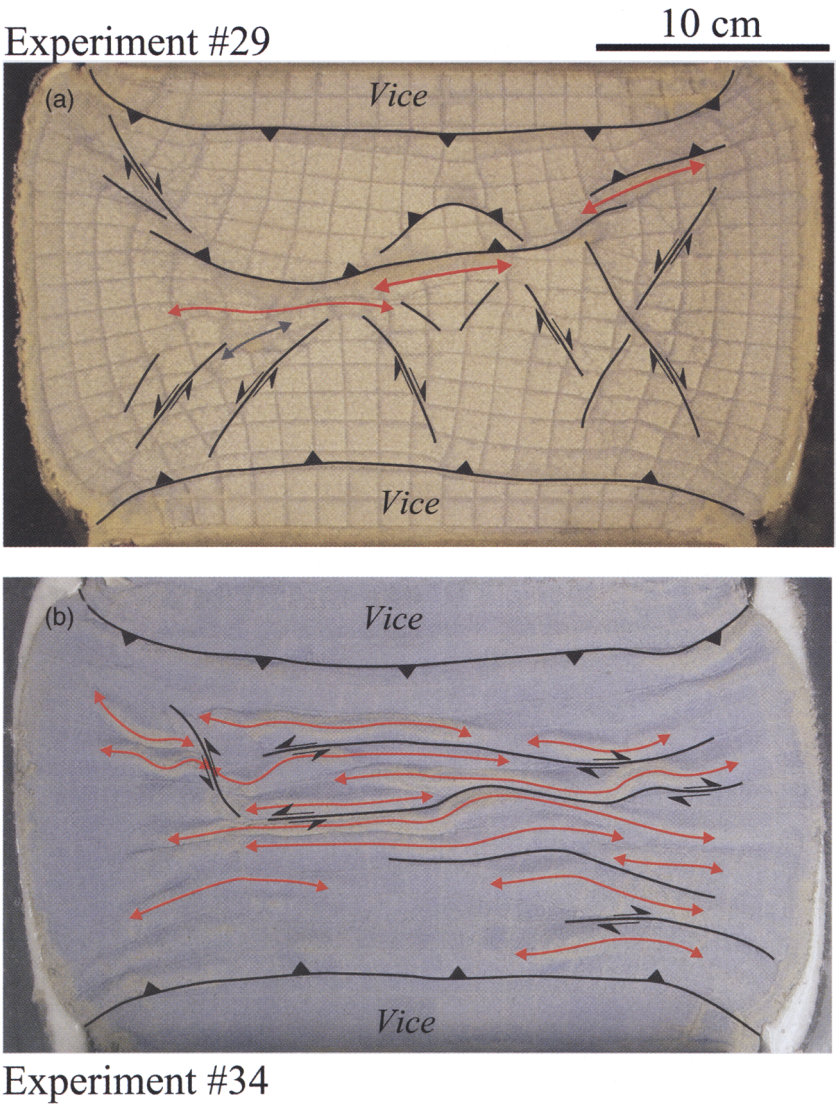

Fig. 7. Structural interpretations of Experiments #29 (**a**) and #34 (**b**), based on surface deformation patterns and serial sections. Red double headed arrows are axial traces of anticlines. Black lines are faults (barbs on hanging wall of thrusts, based on analysis of serial sections; sense of shear on vertical strike slip faults is indicated, based on deflection of marker grid).

vice blocks is more pronounced in the analogue models because of the finite width of the vice blocks over which this torque acts.

Non-buoyant lower crust experiments (#27, #30, #32 and #34)

Results for Experiment #34 are presented in Figures 7 to 9. Although the *Ar* numbers and general topographic growth behaviour are similar (Table 1, Fig. 5), upper crustal deformation in this experiment is markedly different to that in Experiment #29. Namely, the deformation is characterized by the formation of distributed orogen subparallel curvilinear folds from an early stage of the tectonic evolution (Figs 9a, b, c). As shortening progresses the folds lengthen and merge, and at late stages, orogen subparallel shear zones develop,

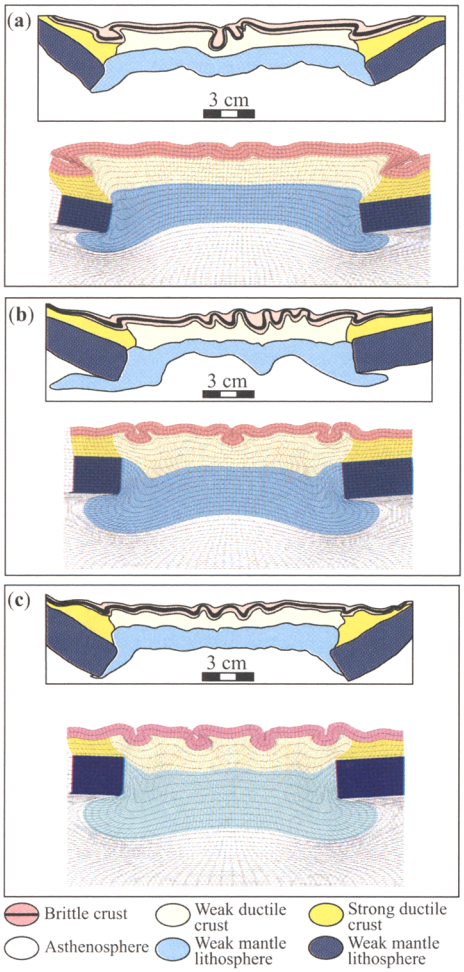

Fig. 8. Central cross-sections for analogue and numerical Experiments #29 (**a**), #34 (**b**) and #32 (**c**) after 32% shortening. Cross-sections of analogue experiments are line drawings traced from photographs of serial sections cut through the centre of the model after freezing.

typically in synclinal cores (Figs 7b and 9d). Conjugate shear zones are generally absent, except at the outer regions of the extruding orogen. The degree of overthrusting of orogenic crust over each vice is significantly less than in models with buoyant crust. Both the amplitude and wavelength of upper crustal folds, as determined from topographic profiles and cross-sections, are quite similar in the analogue and numerical runs.

In experiments with non-buoyant ductile crust, orogen parallel shear zones appear to be favoured in models with thicker brittle upper crust and lower *Ar*, being best developed in Experiment #27 and least well developed in Experiment #32. The geometry of folds at the brittle-ductile boundary also varies according to the effective viscosity of the lower crust. In Experiments #27, #30 and #32 both analogue and numerical runs are characterized by folds at the brittle-ductile interface that are cylindrical in cross-section, with a tendency to develop cuspate geometries in anticlinal cores (Fig. 8c). In Experiment #34, which had a ductile crust an order of magnitude weaker than the other models, anticlinal cores were markedly cuspate, resembling mullion structures in cross-section (Fig. 8b) (e.g., similar to the observations of Sokoutis 1990).

Effects of three-dimensional versus two-dimensional geometry

As noted in the experimental results described above, both the topographic profiles and cross-sections for equivalent analogue and numerical experiments are qualitatively (e.g., fold shapes, vice margin structure; Fig. 8) and quantitatively similar (e.g., close correspondence in amplitude and wavelength of fold-related features on topographic profiles; Figs 6 and 9). However, significant differences between the 3D analogue and 2D numerical experiments are evident when surface deformation patterns are examined (Fig. 7) and in the topographic and internal characteristics of experiments with higher *Ar* numbers (Figs 8c and 10).

The upper crust of the numerical experiments responds to the imposed convergence by folding, and varying amounts of overthrusting at the vice margins. As noted previously, the upper crust of the analogue models is characterized by the development of folds *and* vertical shear zones, either in the form of conjugate arrays (Expts #29 & #33; Fig. 7a) or orogen parallel curvilinear shear zones (Expts #27, #30, #32, #34; Fig. 7b). Thrusts also develop at the vice margins and in some cases in association with pop-up structures formed in the interior of the orogen (e.g., Figs 7a and 8a).

While the lower occurrence of strain localization in the brittle crust of the numerical models can be attributed to choice of model rheology, the development of systems of vertical shear zones in the analogue experiments are due to both strain softening within the granular material *and* orogen-parallel flow. In the case of models with non-buoyant ductile crust, orogenic shortening is accommodated by distributed upper crustal folding and moderate overthrusting

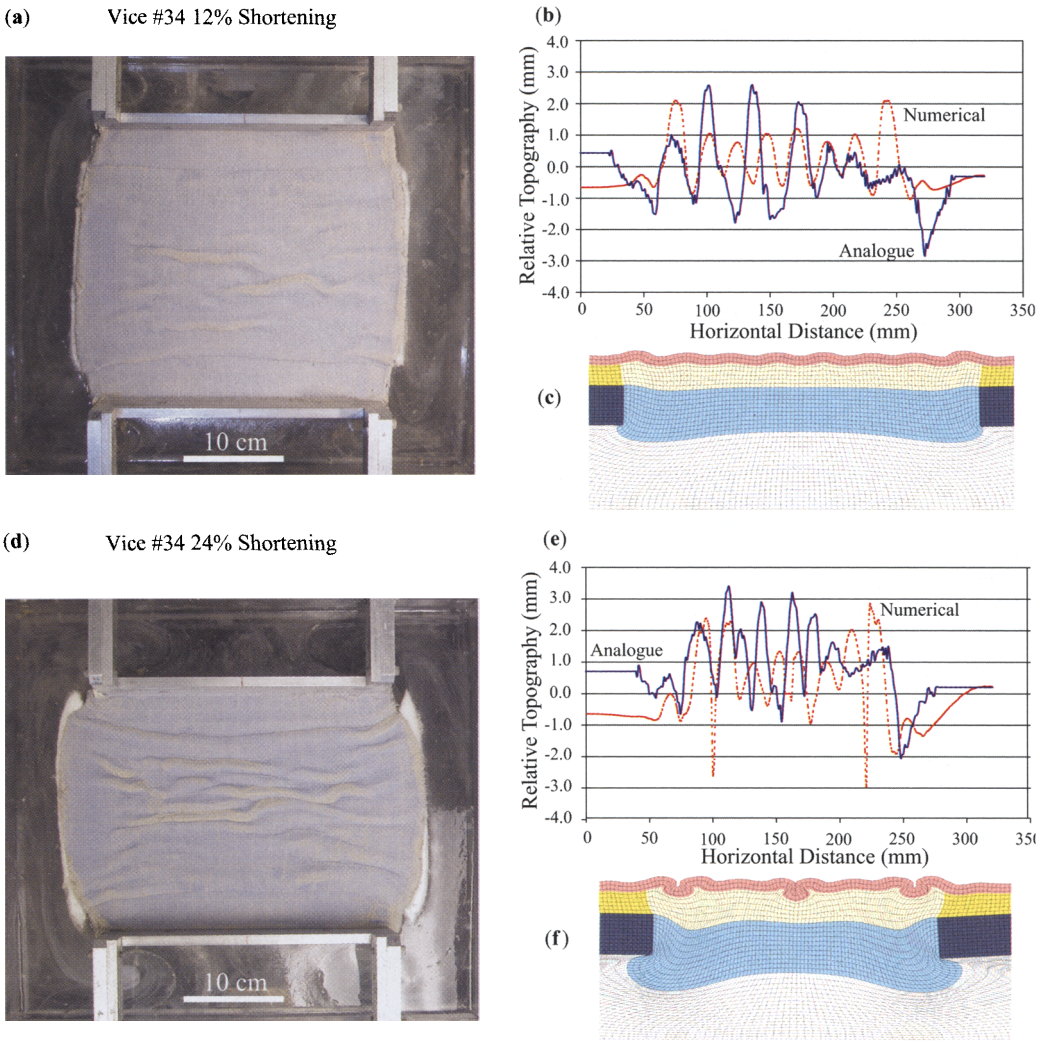

Fig. 9. Results for Experiment #34, with non-buoyant, weak ductile crust. (**a**) and (**d**) Photographs of top surface after 12% and 24% shortening. (**b**) and (**e**) Comparison of central topographic profiles of analogue and numerical models after 12% and 24% shortening. Relative topography is the difference between the present and original elevation. The analogue and numerical results have been re-levelled for comparison purposes. (**c**) and (**f**) Cross-sections of numerical experiment at 12% and 24% shortening.

at vice margins. Orogen-parallel extension in the upper crust of these experiments is taken up by a component of homogeneous stretching, parallel to fold axes and by displacements on orogen subparallel curvilinear shear zones (Fig. 7b). An interesting property of these shear zones is that their sense of shear changes along strike in response to the flow direction in the underlying ductile crust and upper mantle.

In models with buoyant ductile crust, the upper crust responds to convergence by significant overthrusting at vice margins and by localized folding and thrusting in the model interior. Orogen parallel extension in these cases is taken up by relative outward displacements and rotations of large blocks of brittle model upper crust bound by conjugate sets of shear zones, whose acute bisectors are parallel to the convergence direction (Fig. 7a). This style of deformation is attributed to the 3D nature of the 'water bed effect' discussed above. Because the upper crust is lifted up by the buoyant, thickening

ductile crust, it is relatively less confined than in experiments with non-buoyant ductile crust. With the exception of a central region of orogen parallel folds and thrusts, this allows the upper crust to break up into relatively undeformed blocks whose motion between conjugate shear zones is controlled by the flow of the underlying ductile crust and upper mantle (Fig. 7a).

In experiments with low to intermediate *Ar* number (#27, #29, #34) we observe a generally close correspondence between analogue and numerical runs in terms of cross-sectional geometry and topographic profiles, when compared to the central part of the models. However, in the analogue models the mean elevation, the amplitude of folds in cross-section and their surface expression decrease outward along the strike of the orogen, introducing significant differences with respect to the numerical results. These effects are due to the increasing importance of orogen-parallel flow on the geometry of upper crustal structure towards the free end of the models. A similar difference between analogue and numerical results is observed even in the central region of models with high *Ar* number (#32, #33). In these experiments both the amplitudes of folds in cross-section and their surface expression in topographic profiles are noticeably less in the analogue models (Figs 8c and 10). This is because in the analogue experiments with high *Ar* number, gravity driven orogen parallel flow can effectively keep up with the slow imposed convergence rate. In 3D this enhanced outward flow has the effect of suppressing the build up of relief and the amplitude of upper crustal folds, even in the central region of the models.

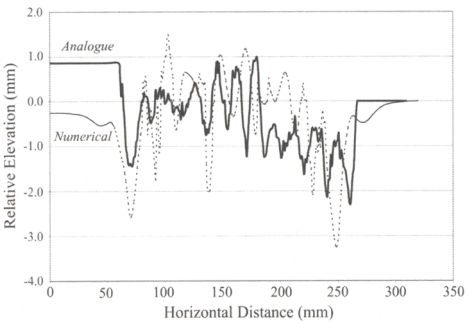

Fig. 10. Relative surface elevation profiles in analogue (central profile; heavy line) and numerical (thin dashed line) runs of Experiment #32. Re-levelled for comparison purposes.

Three-dimensional structure of the brittle-ductile interface

The complex 3D structure of the brittle-ductile interface in the analogue experiments was observed by removal of the upper crustal granular layer with a vacuum hose at the end of each experiment (Fig. 11). Folds at this interface are typically doubly plunging and display an anastomosing pattern in 3D. Fold amplitude and wavelength decreases approaching the free end of the model orogen and the overall strain pattern is similar to that observed in viscous-only experiments (e.g., Fig. 4 and Gilbert & Merle 1987). Significant stretching parallel to fold axes in our experiments is evident from the observation of segmented (boudinaged) fold hinges (Fig. 11). Vertical upper crustal shear zones do not penetrate into the ductile crust, although some shear zones do root into linear zones of very short wavelength, short axial length arrays of en-echelon folds. The brittle-ductile interface therefore represents a decoupling horizon for shear zones, but not for folds, which are clearly continuous across it. However, cross-sections (Fig. 8) show that folding of the brittle ductile interface does not continue to the crust-mantle boundary, indicating that upright folds in the models are disharmonic at the crustal scale.

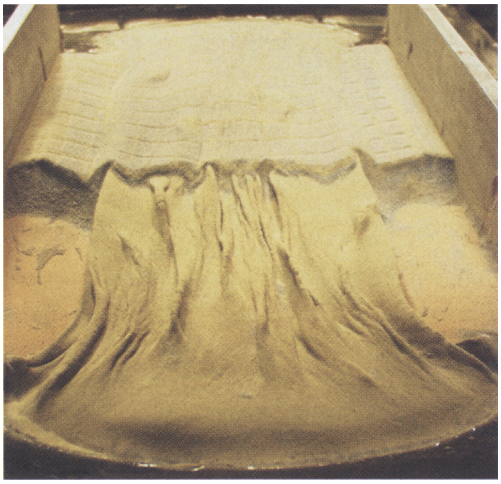

Fig. 11. Oblique view of the brittle-ductile interface (in foreground) of Experiment #27, after removal of upper granular layer (in background) with a vacuum hose. The width of the model between the vertical pistons is 9.6 cm. Strong vice ductile crust is pink, weak ductile crust is yellow.

Three-dimensional bulk finite strains

Comparison of the analogue and numerical experiments indicates that the centre profile cross-sectional area of the ductile crust and orogenic upper mantle in the analogue models has decreased over the duration of each set of runs. The change in cross-sectional area of these layers is an indication that material has flowed out of the section, parallel to the orogen, and is therefore a measure of orogen-parallel stretch in the models.

Using the coordinate system defined in Figure 12a, we employ the change in cross-sectional area of the ductile crust and orogenic upper mantle, together with known amounts of horizontal shortening, to estimate the bulk finite strain in the central portion of each analogue experiment. The principal strains $(1+e_x)$, $(1+e_y)$ and $(1+e_z)$ are defined to be oriented parallel to the shortening direction (x), the orogen (y) and normal to the model surface (z) and the principal strain ratios in this coordinate system are $R_{xy} = (1+e_x)/(1+e_y)$, $R_{xz} = (1+e_x)/(1+e_z)$ and $R_{yz} = (1+e_y)/(1+e_z)$ (Fig. 12a). The bulk principal strain measured parallel to the shortening direction is given by the known amount of convergence in each experiment, $(1+e_x) = [1+(W-W_o)/W_o]$ where W and W_o are the final and original widths of the orogen. The bulk principal strain measured parallel to the orogen can be estimated from the change in cross-sectional area of the unit in question as $(1+e_y) = A_o/A$ where A_o and A are the initial and final cross-sectional areas measured from digital images of serial sections. Assuming the model materials are incompressible, the vertical bulk principal strain is $(1+e_z) = 1/[(1+e_x)(1+e_y)]$, which can be checked against measurements of the change in vertical thickness of the unit from serial sections.

Values of R_{yz} and R_{xz} mantle lithosphere and ductile crust are plotted against Ar in Figures 12b and c. Because of variations between strain ratios estimated for different serial sections, the values presented here are averages determined from bulk strains measured from serial sections in the inner two-thirds of the orogen (i.e., from profiles taken from the centre to two-thirds of the way out to the free edge). Data from the outer one-third has been omitted because strains in this region are highly variable and sensitive to the presence of the unconfined boundary.

The bulk strain ratios in Figure 12 provide a general view of the state of 3D finite strain within the models and therefore can be used to predict fabric elements in the ductile parts of natural vice orogens. Values of R_{yz} increase with increasing Ar, reflecting the greater amount of orogen parallel flow in models with slower shortening rates and larger buoyancy forces (Fig. 12b). For each experiment, R_{yz} is greater in the mantle lithosphere compared to the ductile crust. This reflects the presence of a vertical, orogen-parallel velocity gradient in the models, with the fastest rate of orogen parallel flow occurring at the base of the mantle lithosphere and the slowest at the brittle-ductile interface.

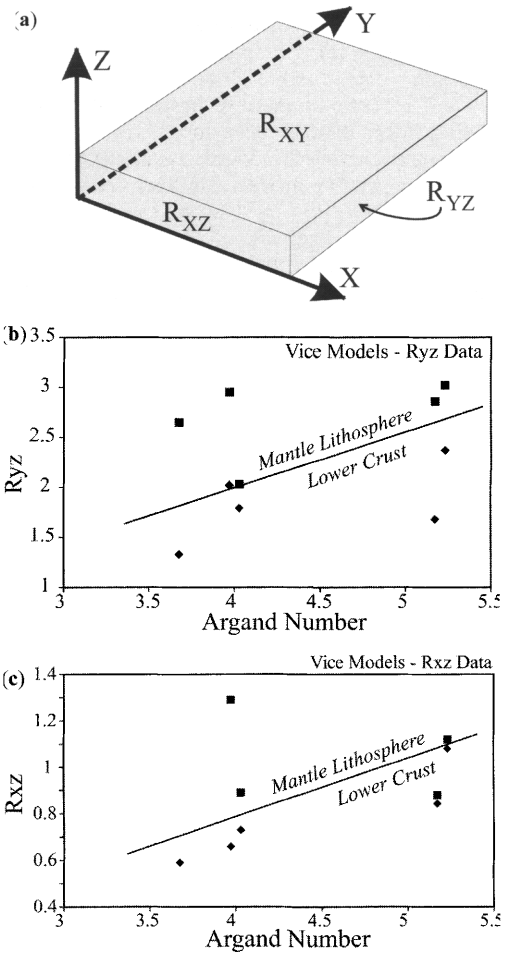

Fig. 12. (**a**) Coordinate system used for determination of bulk strains in analogue models. (**b**) R_{xy} versus Ar number for ductile crust and mantle lithosphere. (**c**) R_{xz} versus Ar number. Squares are bulk strain rations measured for mantle lithosphere, diamonds are ductile crust.

Values of $R_{xz} > 1$ indicate strain ellipsoids with horizontal $(1 + e_x)$ principal strains, while values <1 correspond to strain ellipsoids with vertical $(1 + e_z)$ principal strains. Because of the orogen parallel orientation of $(1 + e_y) > (1 + e_x)$, bulk flattening planes in the ductile crust and mantle lithosphere in the models are therefore either horizontal ($R_{xz} > 1$) or vertical and striking parallel to the orogen ($R_{xz} < 1$). In cases where $R_{xz} = 1$, the bulk strain ellipsoid will be prolate, with a long axis parallel to the orogen. R_{xz} values increase with increasing *Ar*. This is because vertical thinning, $(1 + e_z)$, due to orogen parallel flow, becomes more important with increasing *Ar*. In individual experiments R_{xz} is consistently greater in the mantle lithosphere than in the ductile crust, which again reflects the orogen-parallel vertical velocity gradient.

With exception of Experiment #33 ($Ar = 5.2$), comparison of R_{xz} and R_{yz} values indicates that bulk finite strains in the ductile crust are characterized by vertical orogen-parallel flattening planes with a strong orogen parallel stretch. In Experiment #33, which has the largest Ar number and a buoyant ductile crust, the bulk finite strain is close to prolate orogen parallel stretching in both the ductile crust and mantle lithosphere. Bulk finite strains in the mantle lithosphere in the other experiments vary from close to prolate with strong orogen parallel stretch to general flattening with a horizontal *xy* plane. Bulk plane strains are not observed in any of the analogue models, in contrast to the 2D numerical experiments, which predict, by definition, plane strains.

Local variation in finite strain

The above analysis is useful for predicting the bulk strain symmetry and intensity in the ductile crust and mantle lithosphere of laterally flowing vice orogens. However, examination of analogue model cross-sections (e.g., Fig. 8) and detailed local measurements of local thickness variations in these sections, indicate considerable heterogeneity in finite strain. Although the bulk finite strain in the ductile crust of most models is characterized by a vertical orogen parallel flattening plane, thickness variations indicate that local finite strain in this layer can vary between horizontal flattening and orogen parallel stretching to pure orogen parallel constriction. For example, R_{xz} in Experiment #29 varies locally between 0.35 and 2.6, due entirely to strong vertical thickening (maximum $(1 + e_z) \sim 1.8$) and pronounced vertical thinning (minimum $(1 + e_z) \sim 0.23$) within an individual cross-section. Similar local finite strains are observed in all analogue experiments, indicating that deformation of the ductile crust and mantle lithosphere is characterized by strong across and along-strike variability.

Summary of experimental findings

The major 3D structural characteristics of the vice models, as deduced by analysis of surface deformation patterns, topography data and cross-sections, are summarized in Figure 13. The major finding of the analogue and numerical experiments are as follows:

(1) 3D analogue models highlight the profound effect that syn-convergent orogen parallel flow can have on the development of structures at different levels of the crust (Fig. 13). The significance of these effects is highlighted by comparison to complementary 2D numerical experiments.
(2) Upper crustal deformation is decoupled from lower crustal strain. The boundary between these deformation regimes is transitional and occurs below the brittle-ductile interface in the models.
(3) Finite strain in the ductile crust and mantle lithosphere is characterized by orogen parallel stretching. Strain symmetries vary from horizontal flattening, to orogen parallel constriction, to vertical flattening normal to the shortening direction.
(4) Different upper crustal deformation styles are developed in models with non-buoyant versus buoyant lower crust. Due to the 'water bed' effect, models with buoyant lower crust display marked overflow of the orogenic crust over the bounding vice

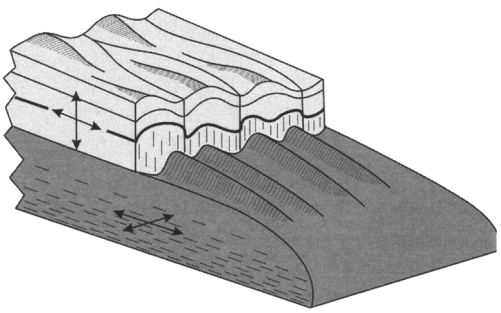

Fig. 13. Interpretation of the first order 3D structural characteristics of the vice experiments. Brittle upper crust is pale grey, ductile crust is dark grey. Arrows indicate orientation of bulk flattening strain (*xy*). Dashes indicate predicted orientation of metamorphic foliations.

blocks, while orogen parallel extension in the upper crust is accommodated by conjugate fracture systems and block rotations. Models with non-buoyant lower crust experience distributed upper crustal folding, and orogen parallel flow in the brittle crust is accommodated by a combination of homogenous stretching and displacements on vertical curvilinear transpression zones, whose kinematics are governed by the polarity of lower crustal flow, rather than the tectonic boundary conditions.

(5) The contribution of gravitational forces to the 3D evolution of the orogen increases with increasing *Ar* number. The *Ar* number controls the mean elevation attained by the orogen and the degree to which orogen-parallel flow will influence the cross-sectional geometry of the orogen. Comparison of analogue and numerical experimental results show that, in the central part of the orogen, amplitudes of folds and their surface expressions are similar in analogue and numerical models with lower *Ar*, while enhanced orogen-parallel flow in analogue models with higher *Ar* results in significant suppression or damping of these structures.

Discussion

Implicit in the vice orogen concept is that the orogenic lithosphere is effectively decoupled from the mantle dynamics responsible for continued plate convergence (Ellis *et al.* 1998). Decoupling of the overriding orogen from the subducting plate appears to be favoured at late stages of collision, provided the orogenic crust becomes sufficiently weak due to the combined effects of thickening and build-up of radiogenic heat (Burg & Ford 1997; Ellis *et al.* 1998). Many large orogens record a similar evolution from initial accretion and collision leading to crustal thickening, followed by gravitationally driven collapse (Dewey *et al.* 1986; Malavieille 1993). In cases where radiogenic heating is great enough, partial melting of the mid to lower crust may occur, leading to enhanced decoupling and the possibility of local buoyancy effects due to the presence of low density felsic melts at depth (Rey 1993; Vanderhaeghe & Teyssier 2001). Hence, the structural and geophysical characteristics of many large orogens are dominated by boundary conditions and mechanical properties that developed at late stages of their history, rather than during the early subduction-related stages of accretion and initial thickening (e.g., Burg *et al.* 2002). The results of the vice model experiments reported above should therefore be evaluated in terms of their potential application to the late-stage structure and dynamics of large hot orogens. Key features of several natural vice orogens are reviewed below in light of the experiments.

The Superior vice: insights from project Lithoprobe

The Superior Province of Canada is thought to have formed by progressive Neoarchean north to south accretion of juvenile volcanic arcs and continental crustal fragments onto a Mesoarchean nucleus (Williams 1990). The large-scale east-west belt structure of the Superior Province (Fig. 14), a variety of syn-accretionary plutonic and sedimentary rocks, together with the preservation of north dipping intra-crustal seismic fabrics and upper-mantle penetrating reflectors, records this *c.* 2720 to 2680 Ma accretionary history (e.g., Card & Ciesielski 1986; Calvert *et al.* 1995; White *et al.* 2003). The post-accretionary history of the Superior province is characterized by widespread granitic intrusion and the development of regional systems of upper crustal, vertical curvilinear shear zones (Fig. 14) (Leclair *et al.* 1993; Card & Poulsen 1998). This late (2660 to 2650 Ma) orogen-scale tectonothermal event coincides with final collision with a continental terrane in the south (Percival *et al.* 1994), thereby putting the entire Superior orogen into the jaws of a north-south vice.

Although generally interpreted in terms of a dextral transpressive regime (e.g., Williams *et al.* 1992), the regional-scale system of curvilinear shear zones have both dextral and sinistral horizontal displacements, depending on their orientation, and typically also record a strong zone normal flattening component (e.g., Wilkinson *et al.* 1999). Seismic reflection profiles indicate that the shear zones root into or are truncated by strong mid-crustal reflectivity fabrics (Jackson & Cruden 1995; Chroukroune *et al.* 1997; White *et al.* 2003). Field observations of tilted crustal sections indicate that mid-crustal reflectivity likely correlates with strong metamorphic fabrics and intrusive layering associated with an episode of east-west extensional flow under high temperature (amphibolite to granulite facies) conditions (Moser *et al.* 1996). U–Pb dating of metamorphic and igneous minerals associated with these fabrics and metamorphic mineral assemblages in upper crustal shear zones indicate that both mid-crustal extensional

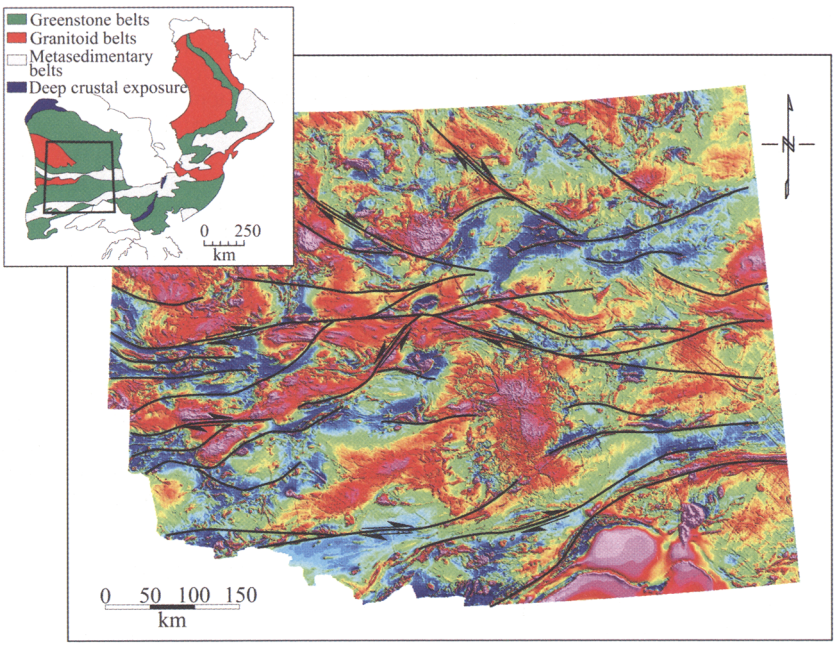

Fig. 14. Total field aeromagnetic map of the western part of the Superior Province (reprocessed after Gupta 1991). Blue tones are low magnetic intensity and red tones are high magnetic intensity. Major curvilinear shear zones, active in the late Archean (*c.* 2680–2650 Ma) are indicated with their sense of horizontal shear, where known. Inset: major subdivisions and location of the Superior Province with respect to the Great Lakes and Hudson's Bay. Box indicates location of the aeromagnetic map.

flow and upper-crustal deformation localized on transpressional shear zones were broadly contemporaneous at *c.* 2660 Ma (Moser *et al.* 1996; Wilkinson *et al.* 1999). Mid-crustal metamorphism continued episodically until *c.* 2600 Ma (Krogh 1993), suggesting that mid to lower crustal flow continued well after upper crustal deformation was locked in.

The geometry, kinematics and timing of upper crustal curvilinear shear zones in the Superior Province and their relationship to mid-crustal, orogen parallel extensional fabrics strongly resembles the characteristics of vice models with non-buoyant lower crust (Fig. 7b). The predominance of low pressure – low to medium temperature metamorphic assemblages within the Superior Province and the local preservation of prehnite-pumpellyite facies rocks indicate that orogenic relief and crustal thickening was likely suppressed. This scenario is most consistent with Experiment #33, which due to a high *Ar* number of 5.2 only increased in average elevation by *c.* 1 mm (equivalent to *c.* 2600 m) after 35% shortening (Fig. 5b), developed upper crustal curvilinear shear zones and upright folds, and experienced strong bulk mid crustal vertical flattening and orogen-parallel extensional strains (Fig. 12). Continued mid to lower crustal ductile flow in the Superior Province could be accounted for by top-down cooling (and stiffening) of a hot crust during continued orogen-parallel collapse.

Other Archean vice orogens

The vice models also account for the structural features of other Neoarchean orogens. For example, the Yilgarn craton of Australia is also characterized by a system of orogen subparallel curvilinear shear zones that root into mid-crustal horizontal reflectors (e.g., Goleby *et al.* 2002). Structural studies indicate the shear zones are associated with orogen-parallel extension, triggered by weakening due to mid-crustal granite emplacement and subsequent gravitational collapse (i.e., increase in *Ar*) (Davis & Maidens 2003). The characteristics of Experiments #33 and #34 also best match those of the Yilgarn.

In contrast to the Superior and Yilgarn, late Archean deformation in the Dharwar craton, India, and Zimbabwe craton, Africa, are strongly

influenced by buoyancy effects in addition to the formation of upper crustal shear zones and folds (Choukroune *et al.* 1997; Treloar & Blenkinsop 1995). The structural style of the Dharwar craton is characterized by an anastomozing system of orogen sub-parallel shear zones which tend to be associated with synformal keels that wrap around elongate doubly plunging antiforms (domes) cored by granitic gneisses. Bouhallier *et al.* (1995) ascribe this strain pattern to lateral compression of thermally weakened lithosphere and simultaneous growth of gravity instabilities in the crust (diapirism). Such a scenario fits well with Experiment #32, which due to the combination of a buoyant lower crust and high *Ar* number, developed orogen sub-parallel shear zones that nucleated in syncline cores, and elongate anticlines cored and amplified by buoyant lower crustal material. Late Archean deformation of the Zimbabwe craton occurred due to compression caused by collision with the central zone of the Limpopo belt to the south (Treloar & Blenkinsop 1995). In contrast to the examples cited above, this led to the development of conjugate sets of regional NNE-striking sinistral and ESE-striking dextral shear zones that accompanied the intrusion of the Chilimanzi granites (Treloar & Blenkinsop 1995). This pattern is consistent with Experiment #29 (Fig. 7a) and suggests that the Chilimanzi granites were sufficiently voluminous to affect the bulk density of the mid crust. However, southward overflow at the Zimbawe craton–Limpopo belt margin is not observed, perhaps due to the protracted earlier tectonic history of this boundary (McCourt & Vearncombe 1992).

Proterozoic vice orogens

Almost all Proterozoic orogens are wide (*c.* 500–1000 km), have significant restored length (>2000 km) and formed by convergence between older, strong Archean lithospheric blocks (e.g., Trans-Hudson orogen, White *et al.* 1999; Svecofennian orogen, Ehlers *et al.* 1993; East African-Antarctic orogen, Jacobs & Thomas 2004). As in the Archean, these orogens record an early history of accretionary tectonics, and are followed by a protracted latter stage of transpression under high temperature conditions (Gapais *et al.* 2005). Taking the Palaeoproterozoic Trans-Hudson orogen of Canada as an example, this late transpression is expressed by orogen sub-parallel curvilinear shear zones and pervasive metamorphic fabrics that record upper crustal vertical thickening and horizontal extension under ductile conditions. Seismic reflection data indicates that vertical upper crustal shear zones root into strong mid-crustal horizontal reflectivity (Hajnal *et al.* 1996). Seismic and structural studies of the eastern boundary of the Trans-Hudson with the Archean Superior Province indicate an early phase of outward thrusting (overflow), followed by steepening and overturning of the boundary zone (White *et al.* 1999). Although the latter feature is not observed in the vice models, the late orogenic structure of the Trans Hudson and other Proterozoic orogens fits well with experiments with non-buoyant lower crust. Given the development of higher pressure metamorphic assemblages and the longevity of high temperature thermal conditions (Gapais *et al.* 2005), Experiment #34 (Figs 7b and 9), with a lower *Ar* number and therefore greater thickening under more ductile lower crustal conditions, applies best to these orogens.

Phanerozoic vice orogens

Elements of vice tectonics can also be recognized in many Palaeozoic to Recent orogenic systems. The original vice models of Ellis *et al.* (1998) were inspired by structural and geophysical features of the Newfoundland Appalachians, where weak lithosphere of the Dunnage zone is squeezed between the strong vice blocks of the Avalon and Humber zones. The Variscan orogeny of Europe developed in response to convergence between Laurentia and Gondwana in the late Palaeozoic (Vanderhaeghe & Teyssier 2001). This convergence led to the development of a major system of orogen sub-parallel curvilinear shear zones and associated sedimentary basins and well-developed mid-crustal horizontal reflectivity linked to partial melting, granite intrusion and extensional flow (Rey 1993; Malavieille 1994; Vanderhaeghe & Teyssier 2001).

Vice tectonics are also apparent in the Alpine-Himalayan system, particularly in Tibet and Anatolia, which are currently experiencing eastward and westward escape in response to collision between Asia with India and Arabia, respectively (Tapponier *et al.* 1982; Dewey *et al.* 1986). As in the vice orogens cited above, orogen parallel extension in the upper crust is accommodated by displacements on systems of curvilinear shear zones that based on available seismic data in Tibet, root into a mid-crust characterized by horizontal reflectivity and the presence of partial melts (Nelson *et al.* 1996; Vanderhaeghe & Teyssier 2001). Although much recent attention has been focussed on orogen perpendicular channel flow of mid-crustal material facilitated by erosion at the southern side of the Himalaya

(e.g., Beaumont *et al.* 2001), the larger scale response of the Tibetan plateau to vice-like convergence between India and Asia is similar to the models presented here and characterized by orogen parallel ductile flow of the lower crust and development of related vertical shear zones in the upper crust (Royden *et al.* 1997).

Likewise, the East Anatolia high plateau appears to be a particularly good example of an active vice orogen. Following an earlier Tertiary accretionary history, this region has experienced vice-like compression between stronger lithospheric blocks represented by the Rhodope-Pontide arc and Arabian plate for the last 11 Ma (Şengör *et al.* 2003). Slab break off at *c.* 11 Ma led to decoupling of the orogenic lithosphere from mantle dynamics as well as crustal weakening and magmatic activity (Keskin 2003). Continued convergence has resulted in the development of the East Anatolia high plateau (mean elevation *c.* 2 km; viz. Experiment #32), significant westward lateral extrusion of the Anatolian block, as well as the development of upper mantle shear wave splitting anomalies that are consistent with orogen parallel flow of the asthenosphere under East Anatolia (Dewey *et al.* 1986; Sandvol *et al.* 2003; Şengör *et al.* 2003).

Implications for fabric studies in orogens

The discussion above focuses on the large-scale surface characteristics and cross-sectional structure of possible vice orogens. Our experiments also provide potential insight on the 3D distribution of strain, fabrics and mesoscopic structures in orogens. For example, field studies find that 'plane strain is more the exception than the rule' in ductilely deformed rocks in orogenic belts (Huddleston 1999) with finite strain measurements indicating a complete spectrum from L-, through L-S and S-tectonites (Ramsay & Huber 1987). The experiments reported here demonstrate that significant variations in finite strain can be achieved by local variation in the degree of vertical thinning or thickening combined with lateral variation in the amount of orogen parallel extension. In particular, they provide insight into the development of orogen parallel stretching lineations observed in the deeper, crystalline parts of some orogens (e.g., Gapais *et al.* 1992; Hatcher 2001) as well as the observation of extension along orogen parallel fold axes (Mancktelow & Pavlis 1994).

A significant feature of all the vice experiments reported here is a transition from upper crustal folding and vertical shear zone development to lower crustal, orogen parallel ductile flow (Fig. 13). The boundary between these regimes in the models is not a discrete detachment; rather it is gradational between the folded brittle-ductile interface and the underlying ductile crust. This is likely an artefact of the model construction: in nature the brittle-ductile transition occurs over a finite thickness of middle crust and field observations indicate that boundaries between 'partitioned' upper and lower crustal structural regimes (Oldow *et al.* 1989; Royden 1996) occur across well-defined detachment structures, often associated with discrete mechanical features such as lithological contacts or magmatic softening horizons (e.g., Collins & Vernon 1991; Axen *et al.* 1998; Klepeis *et al.* 2004).

The common observation of mid to lower crustal seismic reflectivity in orogens is predicted by the orogen parallel flow observed in the models (see also Meissner & Mooney 1998). Because of the weak rheology employed and the vertical velocity gradient observed in the models, orogen parallel stretching is greater in the mantle lithosphere of the experiments than in the ductile crust (Fig. 12b). Strong orogen parallel stretching in the mantle lithosphere and underlying asthenosphere of natural orogens may impart a sufficient degree of anisotropy to cause seismic shear wave splitting anomalies (e.g., Vauchez & Nicolas 1991; Sandvol *et al.* 2003).

Conclusions

Simple vice models provide insight into how different strain regimes can develop at different levels of the crust, in response to boundary conditions, rheological structure and gravitational forces. The experiments provide a framework for the interpretation of a diverse array of structural and geophysical observations in Archean to Recent vice orogens (e.g., upper crustal vs. lower crustal structural regimes; finite strain variation, seismic reflectivity patterns; upper mantle seismic anisotropy). The results also illustrate how in some cases interpretation of local structures in the field (e.g., transpressive shear zones, deep crustal extensional fabrics) might lead to erroneous inferences about palaeotectonic boundary conditions (e.g., oblique convergence; post-orogenic collapse).

The University of Toronto Tectonic Laboratory has been funded by Discovery, Equipment and Lithoprobe Grant programs of the Natural Sciences and Engineering Research Council of Canada (NSERC). We are grateful to D. Boutelier and W. M. Schwerdtner for comments on a draft of the manuscript, and A. Babeyko, S. Ellis and W. Schellart for thorough and constructive reviews, all of which led to substantial improvements, clarifications and corrections. This is Lithoprobe contribution #1412.

References

AXEN, G. J., SELVERSTONE, J., BYRNE, T. & FLETCHER, J. M. 1998. If the strong crust leads, will the weak crust follow? *GSA Today*, **8**, 1–8.

BAILEY, R. C. 1999. Gravity-driven continental overflow and Archaean tectonics. *Nature*, **398**, 413–415.

BAILEY, R. C. 2001. Dynamical analysis of continental overflow. *Journal of Geodynamics* **31**, 293–310.

BEAUMONT, C., JAMIESON, R. A., NGUYEN, M. H. & LEE, B. 2001. Himalayan tectonics explained by extrusion of a low-viscosity crustal channel coupled to focused surface denudation. *Nature*, **414**, 738–742.

BENES, V. & DAVY, P. 1996. Modes of continental lithospheric extension: experimental verification of strain localization processes. *Tectonophysics*, **254**, 69–87.

BLANKENBACH, B. & BUSSE, F. *ET AL.* 1989. A benchmark comparison for mantle convection codes. *Geophysical Journal International*, **98**, 23–38.

BURG, J.-P. & FORD, M. 1997. Orogeny through time: an overview. *In*: BURG, J.-P. & FORD, M. (eds) *Orogeny Through Time*, Geological Society Special Publication, **121**, 1–17.

BURG, J.-P., SOKOUTIS, D. & BONINI, M. 2002. Model-inspired interpretation of seismic structures in the Central Alps: crustal wedging and buckling at mature stage of collision. *Geology*, **30**, 643–646.

BOUHALLIER, H., CHARDON, D. & CHOUKROUNE, P. 1995. Strain patterns in Archaean dome and basin structures: the Dharwar craton (Karnakate, South India). *Earth and Planetary Science Letters*, **135**, 57–75.

CALVERT, A. J., SAWYER, E. W., DAVIS, W. J. & LUDDEN, J. N. 1995. Archaean subduction inferred from a mantle suture in the Superior Province. *Nature*, **375**, 670–674.

CARD, K. D. & CIESIELSKI, A. 1986. DNAG #1 subdivisions of the Superior Province of the Canadian Shield. *Geoscience Canada*, **13**, 5–13.

CARD, K. D. & POULSEN, K. H. 1998. Geology and mineral deposits of the Superior province of the Canadian Shield. *In*: LUCAS, S. B., ST. ONGE, M. R. (eds) *Geology of the Precambrian Superior and Grenville Provinces and Precambrian Fossils of North America*, Geological Society of America, **C1**, 13–204.

CHOUKROUNE, P., BOUHALLIER, H. & ARNDT, N. T. 1995. Soft lithosphere during periods of Archaean crustal growth or crustal reworking. *In*: COWARD, M. P. & REIS, A. C. (eds) *Early Precambrian Processes*, Geological Society Special Publication, **95**, 67–86.

CHOUKROUNE, P., LUDDEN, J. N., CHARDON, D., CALVERT, A. J. & BOUHALLIER, H. 1997. Archaean crustal growth and tectonic processes: a comparison of the Superior Province, Canada and the Dharwar Craton, India. *In*: BURG, J.-P. & FORD, M. (eds) *Orogeny Through Time*, Geological Society Special Publication, **121**, 63–98.

COBBOLD, P. R. & JACKSON, M. P. A. 1992. Gum rosin (colophony): a suitable material for thermomechanical modeling of the lithosphere. *Tectonophysics*, **210**, 255–271.

COLLINS, W. J. & VERNON, R. H. 1991. Orogeny associated with anticlockwise P-T-t paths: evidence from low-P, high-T metamorphic terranes in the Arunta Inlier, central Australia. *Geology*, **19**, 835–838.

DAVIS, B. K. & MAIDENS, E. 2003. Archaean orogen-parallel extension: evidence from the northern Eastern Goldfields Province, Yilgarn Craton. *Precambrian Research*, **127**, 229–248.

DAVY, P. & COBBOLD, P. R. 1988. Indentation tectonics in nature and experiment, 1. Experiments scaled for gravity. *Bulletin of the Geological Institute, University of Uppsala, New Series*, **14**, 129–141.

DAVY, P. & COBBOLD, P. R. 1991. Experiments on shortening of a 4-layer model of the continental lithosphere. *Tectonophysics*, **188**, 1–25.

DEWEY, J. F., HEMPTON, M. R., KIDD, W. S. F., SAROGLU, F. & ŞENGÖR, A. M. C. 1986. Shortening of continental lithosphere: the neotectonics of Eastern Anatolia – a young collision zone. *In*: COWARD, M. P. & RIES, A. C. (eds) *Collision Tectonics*, Geological Society Special Publication, **19**, 3–36.

DIXON, J. M. & SUMMERS, J. M. 1983. Patterns of total and incremental strain in subsiding troughs; experimental centrifuged models of inter-diapir synclines. *Canadian Journal of Earth Sciences*, **20**, 1843–1861.

DIXON, J. M. & SUMMERS, J. M. 1986. Another word on the rheology of silicone putty; Bingham. *Journal of Structural Geology*, **8**, 593–595.

EHLERS, C., LINDROOS, A. & SELONEN, O. 1993. The late Svecofennian granite-migmatite zone of southern Finland – a belt of transpressive deformation and granite emplacement. *Precambrian Research*, **64**, 295–309.

ELLIS, S., BEAUMONT, C., JAMIESON, R. A. & QUINLAN, G. 1998. Continental collision including a weak zone: The vise model and its application to the Newfoundland Appalachians. *Canadian Journal of Earth Sciences*, **35**, 1323–1346.

ENGLAND, P. & HOUSEMAN, G. 1986. Finite strain calculations of continental deformation 2. Comparison with the India-Asia collision zone. *Journal of Geophysical Research*, **91** (B3), 3664–3676.

ENGLAND, P. C. & MCKENZIE, D. P. 1982. A thin viscous sheet model for continental deformation. *Geophysical Journal of the Royal Astronomical Society*, **70**, 295–321.

FULLSACK, P. 1995. An arbitrary Lagrangian-Eulerian formation for creeping flows and its application in tectonic models. *Geophysical Journal International*, **120**, 1–23.

GAPAIS, D., PECHER, A., GILBERT, E. & BALLEVRE, M. 1992. Synconvergence spreading of the higher Himalaya crystalline in Ladakh. *Tectonics*, **11**, 1045–1056.

GAPAIS, D., POTREL, A., MACHADO, N. & HALLOT, E. 2005. Kinematics of long-lasting Palaeoproterozoic transpression within the Thompson Nickel Belt (Manitoba, Canada). *Tectonics*. **24**, TC3002, DOI:10.1029/2004TC001700.

GARDE, A., CHADWICK, B., GROCOTT, J., HAMILTON, M. A., MCCAFFREY, K. J. W. & SWAGER, C. P. 2002. Mid-crustal partitioning and attachment during oblique convergence in an arc system, Palaeoproterozoic Ketilidian orogen, southern Greenland. *Journal of the Geological Society, London*, **159**, 247–261.

GILBERT, E. & MERLE, O. 1987. Extrusion and radial spreading beyond a closing channel. *Journal of Structural Geology*, **9**, 481–490.

GOLEBY, B. R., KORSCH, R. J., FOMIN, T., BELL, B., NICOLL, M. G., DRUMMOND, B. J. & OWEN, A. J. 2002. Preliminary 3-D geological model of the Kalgoorlie region, Yilgarn Craton, Western Australia, based on deep seismic-reflection and potential-field data. *Australian Journal of Earth Sciences*, **49**, 917–933.

GUPTA, V. K. 1991. Shaded image of total magnetic field of Ontario, west central sheet. *Ontario Geological Survey*, Map **M2585**, scale 1:1,000,000.

HAJNAL, Z., LUCAS, S. B., WHITE, D. J., LEWRY, J., BEZDAN, S., STAUFFER, M. R. & THOMAS, M. D. 1996. Seismic reflection images of strike-slip faults and linked detachments in the Trans-Hudson Orogen. *Tectonics*, **15**, 427–439.

HATCHER, R. D. Jr. 2001. Rheological partitioning during multiple reactivation of the Palaeozoic Brevard Fault Zone, Southern Appalachians, USA. *In*: HOLDSWORTH, R. E., STRACHAN, R. A., MAGLOUGHLINE, J. F. & KNIPE, R. J. (eds) *The Nature and Tectonic Significance of Fault Zone Weakening*. Geological Society of London, Special Publications, **186**, 257–271.

HIRT, C. W., AMSDEN, A. A. & COOK, J. L. 1974. An arbitrary Lagrangian-Eulerian computing method for all flow speeds. *Journal of Computational Physics*, **14**, 227–253.

HIRTH, G. & KOHLSTEDT, D. L. 1996. Water in the oceanic upper mantle: implications for rheology, melt extraction and the evolution of the lithosphere. *Earth and Planetary Science Letters*, **144**, 93–108.

HOUSEMAN, G. & ENGLAND, P. 1986. Finite strain calculations of continental deformation 1. Method and general results for convergent zones. *Journal of Geophysical Research*, **91**(B3), 3651–3663.

HOUSEMAN, G. A. & MOLNAR, P. 1997. Gravitational (Rayleigh-Taylor) instability of a layer with non-linear viscosity and convective thinning of continental lithosphere. *Geophysical Journal International*, **128**, 125–150.

HUDLESTON, P. J. 1999. Strain compatibility and shear zones: is there a problem? *Journal of Structural Geology*, **21**, 923–932.

JACKSON, J. 2002. Faulting, flow, and the strength of the continental lithosphere. *International Geology Review*, **44**, 39–61.

JACKSON, S. & CRUDEN, A. R. 1995. Formation of the Abitibi greenstone belt by arc-trench migration. *Geology*, **23**, 471–474.

JACOBS, J. & THOMAS, R. J. 2004. Himalyan-type indenter-escape tectonics model for the southern part of the late Neoproterozoic-early Palaeozoic East African-Antarctic orogen. *Geology*, **32**, 721–724.

KESKIN, M. 2003. Magma generation by slab steepening and breakoff beneath a subduction-accretion complex: an alternative model for collision-related volcanism in Eastern Anatolia, Turkey. *Geophysical Research Letters*, **30**, 8046, DOI 10.1029/2003GL018019.

KLEPEIS, K. A., CLARKE, G. L., GEHRELS, G. & VERVOORT, J. 2004. Processes controlling vertical coupling and decoupling between the upper and lower crust of orogens: results from Fiordland, New Zealand. *Journal of Structural Geology*, **26**, 765–791.

KOHLSTEDT, D. L., EVANS, B. & MACKWELL, S. J. 1995. Strength of the lithosphere: constraints imposed by laboratory experiments. *Journal of Geophysical Research*, **100**, 17587–17602.

KROGH, T. E. 1993. High precision U-Pb ages for granulite metamorphism and deformation in the Archean Kapuskasing structural zone, Ontario: implications for structure and development of the lower crust. *Earth and Planetary Science Letters*, **119**, 1–18.

LECLAIR, A. D., ERNST, R. E. & HATTORI, K. 1993. Crustal-scale auriferous shear zones in the central Superior province, Canada. *Geology*, **21**, 399–402.

MACKWELL, S. J., ZIMMERMAN, M. E. & KOHLSTEDT, D. L. 1998. High-temperature deformation of dry diabase with application to tectonics on Venus. *Journal of Geophysical Research*, **103** (B1), 975–984.

MAGGI, A., JACKSON, J. A., MCKENZIE, D. & PRIESTLEY, K. 2000. Earthquake focal depths, effective elastic thickness, and the strength of the continental lithosphere. *Geology*, **28**, 495–498.

MALAVIEILLE, J. 1993. Late orogenic extension in mountain belts: insights from the Basin and Range and the late Paleozoic Variscan belt. *Tectonics*, **12**, 1115–1130.

MANCKTELOW, N. S. & PAVLIS, T. L. 1994. Fold-fault relationships in low-angle detachment systems. *Tectonics*, **13**, 668–685.

MCCOURT, S. & VEARNCOMBE, J. R. 1992. Shear zones of the Limpopo Belt and adjacent granitoid-greestone terranes: implications for late Archaean collision tectonics in southern Africa. *Precambrian Research*, **55**, 553–570.

MEISSNER, R. & MOONEY, W. 1998. Weakness of the lower continental crust: a condition for delamination, uplift and escape. *Tectonophysics*, **296**, 47–60.

MITROVICA, J. X. & FORTE, A. M. 1997. The radial profile of mantle viscosity: results from the joint inversion of convection of post-glacial rebound observables. *Journal of Geophysical Research*, **102**, 2751–2769.

MERLE, O. 1989. Strain models within spreading nappes. *Tectonophysics*, **165**, 57–71.

MOSER, D. E., HEAMAN, L. M., KROGH, T. E. & HANES, J. A. 1996. Intracrustal extension of an Archean orogen revealed using single-grain U-Pb geochronology. *Tectonics*, **15**, 1093–1109.

NELSON, K. D. and ZHAO, W. *ET AL.* 1996. Partially molten middle crust beneath southern Tibet:

synthesis of project INDEPTH results. *Science*, **274**, 1684–1688.

OLDOW, J. S., BALLY, A. W., Avé LALLEMANT, H. G. & LEEMAN, W. P. 1989. Transpression, orogenic float, and lithospheric balance. *Geology*, **18**, 991–994.

PERCIVAL, J. A., STERN, R. A., SKULSKI, T., CARD, K. D., MORTENSEN, J. K. & BÉGIN, N. J. 1994. Minto block, Superior province: missing link in deciphering assembly of the craton at 2.7 Ga. *Geology*, **22**, 839–842.

POLIAKOV, A. & PODLADCHIKOV, Y. 1992. Diapirism and topography. *Geophysical Journal International*, **109**, 553–564.

PYSKLYWEC, R. & CRUDEN, A. R. 2004. Coupled crust-mantle dynamics and intraplate tectonics: two-dimensional numerical and three-dimensional analogue modelling. *Geochemistry, Geophysics, Geosystems (G^3)*, **5**(10), Q10003, DOI 10.1029/2004GC000748.

RAMSAY, J. G. & HUBER, M. I. 1987. *The techniques of modern structural geology. Volume 2. Folds and Fractures.* Academic Press.

RATSCHBACHER, L., MERLE, O., PHILLIPE, D. & COBBOLD, P. 1991. Lateral extrusion in the Eastern Alps: Part I. Boundary conditions and experiments scaled for gravity. *Tectonics*, **10**, 245–256.

REY, P. 1993. Seismic and tectono-metamorphic characters of the lower continental crust in Phanerozoic areas: a consequence of post-thickening extension. *Tectonics*, **12**, 580–590.

REY, P., VANDERHAEGHE, O. & TEYSSIER, C. 2001. Gravitational collapse of continental crust: Definitions, regimes, mechanisms and modes. *Tectonophysics*, **342**, 435–449.

ROSS, G. M., MILKEREIT, B., EATON, D., WHITE, D., KANASEWICH, E. R. & BURIANYK, M. J. A. 1995. Palaeoproterozoic collision orogen beneth the western Canada sedimentary basin imaged by Lithoprobe crust seismic-reflection data. *Geology*, **23**, 195–199.

ROSSI, D. & STORTI, F. 2003. New artificial granular materials for analogue laboratory experiments: aluminium and siliceous microspheres. *Journal of Structural Geology*, **25**, 1893–1899.

ROYDEN, L. 1996. Coupling and decoupling of crust and upper mantle in convergent orogens: implications for strain partitioning in the crust. *Journal of Geophysical Research*, **101**(B8), 17679–17705.

ROYDEN, L., BURCHFIEL, B. C., KING, R. W., WANG, E., CHEN, Z., SHEN, F. & LIU, Y. 1997. Surface deformation and lower crustal flow in eastern Tibet. *Science*, **276**, 788–790.

SANDVOL, E. & TURKELLI, N. *ET AL.* 2003. Shear wave splitting in a young continent-continent collision: An example from Eastern Turkey. *Geophysical Research Letters*, **30**, 8041, DOI 10.1029/2003GL017390.

SCHELLART, W. P. 2000. Shear test results for cohesion and friction coefficients for different granular materials: scaling implications for their usage in analogue modelling. *Tectonophysics*, **324**, 1–16.

SCHELLART, W. P. & LISTER, G. S. 2004. Tectonic models for the formation of arc-shaped convergent zones and backarc basins. *In*: SUSSMAN, A. J. & WEIL, A. B. (eds) *Orogenic curvature: integrating palaeomagnetic and structural analysis*, Geological Society of America Special Paper, **383**, 237–258.

ŞENGÖR, A. M. C., ÖZEREN, S., GENÇ, T. & ZOR, E. 2003. East Anatolia high plateau as a mantle-supported, north-south shortened domal structure. *Geophysical Research Letters*, **30**, 8045, DOI 10.1029/2003GL017858.

SEYFERTH, M. & HENK, A. 2004. Syn-convergent exhumation and lateral extrusion in continental collision zones – insights from three-dimensional numerical models. *Tectonophysics*, **382**, 1–29.

SOKOUTIS, D. 1990. Experimental mullions at single and double interfaces. *Journal of Structural Geology*, **12**, 365–373.

SOKOUTIS, D., BONINI, M., MEDVEDEV, S., BOCCALETTI, M., TALBOT, C. J. & KOYI, H. 2000. Indentation of a continent with a built-in thickness change: experiment and nature. *Tectonophysics*, **320**, 243–270.

TAPPONNIER, P., PELTZER, G., LA DAIN, A. Y., ARMIJO, R. & COBBOLD, P. 1982. Propagating extrusion tectonics in Asia: New insights from simple experiments with plasticene. *Geology*, **10**, 611–616.

TEYSSIER, C. & WHITNEY, D. 2002. Gneiss domes and orogeny. *Geology*, **30**, 1139–1142.

TOUSSAINT, G., BUROV, E. & JOLIVET, L. 2004. Continental plate collision: unstable vs. stable slab dynamics. *Geology*, **32**, 33–36.

TRELOAR, P. J. & BLENKINSOP, T. G. 1995. Archaean deformation patterns in Zimbabwe: true indicators of Tibetan-style crustal extrusion or not? *In*: COWARD, M. P. & REIS, A. C. (eds) *Early Precambrian Processes*, Geological Society Special Publication, **95**, 87–108.

VANDERHAEGHE, O. & TEYSSIER, C. 2001. Partial melting and flow of orogens. *Tectonophysics*, **342**, 451–472.

VAN KEKEN, P. E., KING, S. D., SCHMELING, H., CHRISTENSEN, U. R., NEUMEISTER, D. & DOIN, M. P. 1997. A comparison of methods for the modeling of thermochemical convection. *Journal of Geophysical Research*, **102**, 22477–22496.

VAUCHEZ, A. & NICOLAS, A. 1991. Mountain building: strike-parallel motion and mantle anisotropy. *Tectonophysics*, **185**, 183–201.

WEIJERMARS, R. 1986. Flow behaviour and physical chemistry of bouncing putties and related polymers in view of tectonic laboratory. *Tectonophysics*, **124**, 325–358.

WHITE, D. J., JONES, A. G., LUCAS, S. B. & HAJNAL, Z. 1999. Tectonic evolution of the Superior boundary zones from coincident seismic reflection and magnetotelluric profiles. *Tectonics*, **18**, 430–451.

WHITE, D. J., MUSACCHIO, G., HELMSTAEDT, H. H., HARRAP, R. M., THURSTON, P. C., VAN DER VELDEN, A. & HALL, K. 2003. Images of a lower-crustal oceanic slab: direct evidence for tectonic accretion in the Archean western Superior province. *Geology*, **31**, 997–1000.

WILKINSON, L., CRUDEN, A. & KROGH, T. 1999. Timing and kinematics of post-Timiskaming deformation within the Larder Lake-Cadillac deformation zone, SW Abitibi greenstone belt, Ontario, Canada. *Canadian Journal of Earth Sciences*, **36**, 627–647.

WILLIAMS, H. R. 1990. Subprovince accretion tectonics in the south-central Superior Province. *Canadian Journal of Earth Sciences*, **27**, 570–581.

WILLIAMS, H. R., SCOTT, G. M., THURSTON, P. C., SUTCLIFFE, R. H., BENNET, G., EASTON, R. M. & ARMSTRONG, D. K. 1992. Tectonic evolution of Ontario: Summary and Synthesis. In: *Geology of Ontario*, Special volume **4**, part 2, Ontario Geological Survey, Canada, 1255–1332.